Biomass burning impact on CCN number, hygroscopicity and cloud formation during summertime in the Eastern Mediterranean

A. Bougiatioti[1,2,3], S. Bezantakos[4,5], I. Stavroulas[3], N. Kalivitis[3], P. Kokkalis[2,11], G. Biskos[6,7], N. Mihalopoulos[3,7,10], A. Papayannis[2], A. Nenes[1,8,9,10]

[1]School of Earth and Atmospheric Sciences, Georgia Institute of Technology, Atlanta, GA, USA
[2]Laser Remote Sensing Unit, National Technical University of Athens, Zografou, Athens, Greece
[3]ECPL, Department of Chemistry, University of Crete, Voutes, 71003 Heraklion, Greece
[4]Department of Environment, University of the Aegean, Mytilene, 81100, Greece
[5]Institute of Nuclear Technology and Radiation Protection, NCSR "Demokritos", 15310 Ag. Paraskevi, Athens, Greece
[6]Faculty of Civil Engineering and Geosciences, Delft University of Technology, Delft 2728 CN, The Netherlands
[7]Energy Environment and Water Research Center, The Cyprus Institute, Nicosia 2121, Cyprus
[8]School of Chemical & Biomolecular Engineering, Georgia Institute of Technology, Atlanta, GA, USA
[9]Institute of Chemical Engineering Sciences (ICE-HT), FORTH, Patras, Greece
[10]IERSD, National Observatory of Athens, P. Penteli 15236, Athens, Greece
[11]IAASARS, National Observatory of Athens, P. Penteli 15236, Athens, Greece

Abstract

This study investigates the concentration, cloud condensation nuclei (CCN) activity and hygroscopic properties of particles influenced by biomass burning in the eastern Mediterranean and their impacts on cloud droplet formation. Air masses sampled were subject to a range of atmospheric processing (several hours up to 3 days). Values of the hygroscopicity parameter, κ, were derived from CCN measurements and a Hygroscopic Tandem Differential Mobility Analyzer (HTDMA). An Aerosol Chemical Speciation Monitor (ACSM) was also used to determine the chemical composition and mass concentration of non-refractory components of the submicron aerosol fraction. During fire events, the increased organic content (and lower inorganic fraction) of the aerosol decreases the values of κ, for all particle sizes. Particle sizes smaller than 80 nm exhibited considerable chemical dispersion (where hygroscopicity varied up to 100% for particles of same size); larger particles, however, exhibited considerably less dispersion owing to the effects of condensational growth and cloud processing. ACSM measurements indicate that the bulk composition reflects the hygroscopicity and chemical nature of the largest particles (having a diameter of ~100 nm at dry conditions) sampled. Based on Positive Matrix Factorization (PMF) analysis of the organic ACSM spectra, CCN concentrations follow a similar trend with the biomass burning organic aerosol (BBOA) component, with the former being enhanced between 65 and 150% (for supersaturations ranging between 0.2 and 0.7%) with the arrival of the smoke plumes. Using multilinear regression of the PMF factors (BBOA, OOA-BB and OOA) and the observed hygroscopicity parameter, the inferred hygroscopicity of the oxygenated organic aerosol components is determined. We find that the transformation of freshly-emitted biomass burning (BBOA) to more oxidized organic aerosol (OOA-BB) can result in a twofold increase of the inferred organic hygroscopicity; about 10% of the total aerosol hygroscopicity is related to the two biomass burning components (BBOA and OOA-BB), which in turn contribute almost

35% to the fine-particle organic water of the aerosol. Observation-derived calculations of the cloud droplet concentrations that develop for typical boundary layer clouds conditions suggest that biomass burning increases droplet number, on average by 8.5%. The strongly sublinear response of clouds to biomass burning (BB) influences is a result of strong competition of CCN for water vapor, which results in very low maximum supersaturation (0.08% on average). Attributing droplet number variations to the total aerosol number and the chemical composition variations shows that the importance of chemical composition increases with distance, contributing up to 25% of the total droplet variability. Therefore, although BB burning may strongly elevate CCN numbers, the impact on droplet number is limited by water vapor availability and depends on the aerosol particle concentration levels associated with the background.

1. Introduction

Globally, biomass burning (BB) is a major source of atmospheric aerosols (Andreae et al., 2004). In the eastern Mediterranean, up to one third of the dry submicron aerosol mass during the summer period consists of highly oxidized organic compounds (Hildebrandt et al., 2010). During July-September, biomass-burning aerosol originates from long-range transport from Southern Europe and countries surrounding the Black Sea (Sciare et al., 2008). Bougiatioti et al. (2014) showed that of the total organic aerosol (OA), about 20% is freshly-emitted biomass burning organic aerosol (BBOA), 30% is oxidized, processed OA originating from BBOA (BB-OOA), and the remaining 50% is highly oxidized aerosol that results from extensive atmospheric aging. Hence, in term of organic mass, during time periods of high biomass burning activity, at least 50% of the aerosol can be attributed to BB emissions.

Aerosol liquid water content (LWC) is a key medium for atmospheric chemistry that also drives the partitioning of soluble organic vapors to the particle phase (Carlton and Turpin, 2013). LWC is a prime modulator of aerosol direct radiative forcing (e.g., Pilinis et al., 1995), and by promoting secondary aerosol formation it can influence aerosol mass and number, that impacts both on the aerosol direct and indirect effect (Kanakidou et al., 2005).

Biomass burning aerosol particles have the potential to act as cloud condensation nuclei (CCN), thereby impacting on cloud properties and climate. Modeling studies suggest that BB is a significant global source of CCN number (Spracklen et al., 2011). Laboratory and field studies have shown that biomass burning aerosol is highly hygroscopic and water-soluble, exhibiting up to about half the water uptake capacity of ammonium sulfate (Asa-Awuku et al., 2008; Cerully et al., 2014). Engelhart et al. (2012) found that freshly emitted BBOA displays a broad range of hygroscopicity (κ parameter from 0.06 to 0.6) that considerably reduces after just a few hours of photochemical aging, to a κ value of 0.2±0.1 (Petters and Kreidenweis, 2007). Few studies, however, focus on the hygroscopicity of ambient BB aerosol as a function of atmospheric age extending out to a few days. Relatively few studies also go beyond CCN to calculations of droplet number (e.g., Roberts et al., 2003), and even fewer studies characterize the relative role of aerosol number and chemical composition (hygroscopicity) variability to the predicted droplet number variability in clouds formed from BB-influenced masses. These issues are important, because the supersaturation that develops in clouds is not known beforehand, nor constant, but rather a strong function of the CCN levels and cloud dynamical forcing (updraft velocity).

In the current study we focus on the hygroscopicity, CCN concentrations and resulting droplet formation characteristics (droplet number and cloud supersaturation) associated with air masses influenced by summertime biomass burning events in the eastern Mediterranean. The smoke-laden air masses sampled were subject to a range of atmospheric processing (several hours up to 3 days), identified using remote sensing techniques (Moderate Resolution Imaging Spectroradiometer, Kaufman and Remer, 1994; Cloud-Aerosol Lidar with Orthogonal Polarization, Winker et al., 2009, Mamouri et al., 2012), backtrajectory analysis and other in-situ chemical metrics. Values of the hygroscopicity parameter, κ, were derived from CCN and HTDMA measurements and linked to distinct chemical constituents identified with Positive Matrix Factorization of the chemical constituents measured with an Aerosol Chemical Speciation Monitor (ACSM). Finally, the observations are used to predict the cloud droplet number and supersaturation formed in clouds that develop in each air mass, focusing on the contribution of aerosol number and hygroscopicity to the predicted droplet number variability. This is one of the very few field studies that use in-situ observations to i) unravel the contributions of composition and aerosol size to BB CCN distributions and their impacts on cloud droplet number, ii) quantify the contributions of biomass burning constituents to aerosol hygroscopicity and liquid water in the region.

2. Experimental Methods

2.1 Sampling site and period

The measurements were performed at the Finokalia station (35^{o}32'N, 25^{o}67'E; http://finokalia.chemistry.uoc.gr) of the University of Crete, which is part of the Aerosols, Clouds, and Trace gases Research Infrastructure Network (ACTRIS; http://www.actris.net/). More details about the sampling site are provided by Mihalopoulos et al. (1997) and Sciare et al. (2003). Although measurements took place from mid-August to mid-November 2012, the focus of our analysis involves the periods of intense biomass burning influence, August to September 2012. BB plumes sampled were fresh, originating from the Greek islands and mainland (transport time 6-7 h) but also from long-range transport from the Balkans (transport time > 1 day) as determined by using HYSPLIT backtrajectory analysis as shown in detail in Bougiatioti et al. 2014 combined with the hot spots/fire data from MODIS/Fire Information for Resource Management System (FIRMS; Remy and Kaiser, 2014).

2.2 Instrumentation and methodology

Chemical composition and mass concentration of non-refractory components (ammonium, sulfate, nitrate, chloride and organics) of the submicron aerosol fraction was provided by an Aerodyne Research Aerosol Chemical Speciation Monitor (ACSM; Ng et al., 2011) with a temporal resolution of 30 minutes. More details of the ACSM measurements and subsequent analysis can be found in Bougiatioti et al. (2014). Total absorption measurements provided the black carbon (BC) concentrations by a seven-wavelength aethalometer (Magee Scientific, AE31). From the BC measurements and using the approach of Sandradewi et al. (2008) the wood-burning and fossil fuel contribution to the total BC concentrations were calculated, using an absorption exponent of 1.1 for fossil fuel burning and 1.86 for pure wood burning. The aerosol particle size distributions from 9 to 850 nm were measured with a 5-min resolution by a custom-built scanning mobility particle sizer (SMPS; TROPOS-type, Wiedensohler et al., 2012) equipped with a condensation particle counter (CPC; TSI model 3772; ; Stolzenburg and McMurry, 1991). Sample humidity was regulated below the relative humidity of 40% with the use of Nafion® dryers in both aerosol and sheath flow and the measured umber size distributions were corrected for diffusional particle losses (Kalivitis at al. 2015). A Continuous Flow Stream-wise Thermal Gradient CCN Chamber (CFSTGC; Roberts and Nenes, 2005) was used in parallel with a Hygroscopic Tandem Differential Mobility Analyzer (HTDMA; Rader and McMurry, 1986) to measure the CCN number, activity and hygroscopicity of ambient aerosol for supersaturated (0.1-0.7%) and subsaturated conditions (relative humidity, RH=86%), respectively. The whole system, which is illustrated in Figure 1, sampled air with a total flow-rate of 1.8 L min^{-1}. After passing through a Nafion dryer (MD-110-12S-2, Perma Pure LLC, RH<30%) the dried particles were selected based on their electrical mobility by a Differential Mobility Analyzer (DMA-1;TSI Model 3080; Knutson and Whitby, 1975). The sheath flow and classified aerosol outlet flow of DMA-1 were 10.8 and 1.8 L min^{-1}, respectively, while the mobility diameter was changed every 6 minutes between 60, 80, 100 and 120 nm.

The classified aerosol from DMA-1 was then split into two streams. The first stream was passed through a Nafion-tube humidity exchanger where its RH was increased to 86%. The size distribution of the RH-conditioned particles was determined by a second DMA (DMA-2; custom-made DMA using a closed-loop sheath flow with RH control; Biskos et al., 2006; Bezantakos et al., 2013) coupled with a Condensation Particle Counter (CPC, TSI Model 3772. The RH in both the aerosol and the sheath flow in DMA-2 was controlled by PID controllers to within ±2% accuracy. Both DMAs in the HTDMA system were calibrated with Polystyrene Latex (PSL) spheres. The other classified stream was introduced into the CFSTGC to measure the CCN activity of particles. The CFSTGC was operated in Scanning Flow CCN Analysis (SFCA) mode (Moore and Nenes, 2009), in which the flow rate in the growth chamber changes over time, while a constant streamwise temperature difference is applied. This causes supersaturation to change continuously, allowing the rapid and continuous measurement of CCN spectra with high temporal resolution. The SFCA cycle used involved first increasing the flow rate linearly between a minimum flow rate (Q_{min} ~ 300 cm^3 min^{-1}) and a maximum flow rate (Q_{max} ~ 1000 cm^3 min^{-1}) over a ramp time of 60 seconds. The flow was maintained at Q_{max} for 10 seconds and then linearly decreased to Q_{min} over 60 s. Finally, the flow rate was held constant at Q_{min} for 10 s and the scan cycle was repeated. The activated droplets in the CFSTGC were counted and sized at the exit of its growth chamber with an Optical Particle Counter (OPC) that detects droplets and classifies them into 20 size bins with diameter ranging from 0.7 to 10 μm every 1 s.

The water vapor supersaturations developed in the CFSTGC during an SFCA cycle were characterized with ammonium sulfate calibration aerosol following the procedure of Moore and Nenes (2009). In brief, an ammonium sulfate solution was atomized, dried, charge-neutralized and classified by DMA-1. The resulting monodisperse aerosol flow was split between DMA-2 and the CFSTGC, operating in SFCA mode and with a CFSTGC streamwise temperature difference of ΔT=5 K. From this setup, we obtain the instantaneous concentrations of the classified aerosol and the resulting CCN during the SFCA flow cycles. . The ratio of CCN to total aerosol number gives the activation ratio, R_a, which varies with the instantaneous volumetric flow rate, Q, in the CFSTGC. Using data from multiple SFCA flow cycles, R_a is then fit to a sigmoid function that depends on Q:

$$R_a \equiv \frac{CCN}{CN} = a_o + \frac{a_1 - a_0}{1 + (Q/Q_{50})^{-a_2}} \qquad (1)$$

where a_0, a_1, a_2 and Q_{50}, are constants which describe the minimum, maximum, slope and inflection point of the sigmoidal, respectively. The “critical flow rate”, Q_{50}, corresponds to the instantaneous flow rate that produces a level of supersaturation, s, required to activate the measured monodisperse aerosol. s is determined from the size of the classified aerosol using Köhler theory (Moore et al., 2012a).

.

Repeating the procedure for many sizes of classified ammonium sulfate results in the SFCA calibration curve, which gives the supersaturation in the CFSTGC as a function of flow rate (i.e Q_{50} vs. s) throughout an SFCA flow cycle. Absolute uncertainty of the calibrated CCNC supersaturation is estimated to be ±0.04% (Moore et al., 2012a; 2012b).

In our instrument setup, R_a can change either from variations in the size of the monodisperse aerosol, d_p, or the instrument supersaturation, s (or flow rate, Q). The independently varied parameter is indicated hereon in parentheses in front of the activation ratio, e.g., $R_a(Q)$, $R_a(s)$, $R_a(d_p)$ for R_a as a function of Q, s and d_p, respectively.

Analysis of R_a obtained for our experimental setup for ambient particles samples provide very important information on the activity and chemical mixing state of the CCN. This is carried out as follows. For every particle size d_p set by the DMA-1, $R_a(Q)$, is measured at every instant in the CFSTGC according to Eq.1. Typically $a_0 << a_1$; given that Q and s are related through the calibration, $R_a(Q)$ data can be transformed to R_a (s) as:

$$R_a(s) = \frac{E}{1 + \left(\frac{s}{s^*}\right)^C} \qquad (2)$$

where s, s^* correspond to Q, Q_{50} of the monodisperse aerosol. E, C are parameters determined from fitting. According to Cerully et al., (2011), $R_a(s)$ represents a cumulative distribution of critical supersaturation for particles with dry diameter d_p; Köhler theory can then be applied to express $R_a(s)$ in terms of the hygroscopicity parameter $R_a(\kappa)$:

$$R_a(\kappa) = \frac{E}{1+\left(\frac{\kappa}{\kappa^*}\right)^{C/2}} \qquad (3)$$

where $\kappa = \frac{4\mathrm{A}^3}{27{d_p}^3 s^2}$ is the dependence of κ on d_p and s, $A = \frac{4M_w\sigma_w}{RT\rho_w}$ is the Kelvin parameter, whereas M_w, σ_w and ρ_W are respectively the molar mass, the surface tension and the density of water, R is the universal gas constant, and T is temperature. In equations 2, 3, s^* and κ^* correspond to the characteristic critical supersaturation and hygroscopicity parameter of the monodisperse aerosol, respectively and correspond to the most probably values of the parameters (Cerully et al., 2011). From Equation 3, the probability distribution function for κ, $p^s(\kappa)$, can be derived for the ambient monodisperse aerosol (Cerully et al., 2011):

$$p^s(\kappa) = \frac{1}{E}\frac{dR_a(\kappa)}{d\kappa} = -\frac{\frac{C}{\kappa^* 2}\left(\frac{\kappa}{\kappa^*}\right)^{\frac{C}{2}-1}}{\left(1+\left(\frac{\kappa}{\kappa^*}\right)^{\frac{C}{2}}\right)^2} \qquad (4)$$

Analysis of $p^s(\kappa)$ can provide a direct measure of the chemical heterogeneity of the CCN population. For this, we adopt the metric of chemical dispersion, $\sigma(\kappa)$, introduced by Lance (2007) and further developed in Cerully et al. (2011) and Lance et al. (2013):

$$\sigma^2(\kappa) = \frac{\int_0^1 (\kappa-\kappa^*)^2 p^s(\kappa)d\kappa}{\int_0^1 p^s(\kappa)d\kappa} \qquad (5)$$

$\sigma(\kappa)$ is the square root of variance about κ^*; as the chemical heterogeneity of the CCN increases, the distribution of κ broadens, and $\sigma(\kappa)$ becomes larger so that the range in CCN hygroscopicity is given by $\kappa^* \pm \sigma(\kappa)$.

Particle water uptake at sub-saturated conditions in the Nafion-tube humidity exchanger and DMA-2 was also evaluated by the growth factor measured for the calibration $(NH_4)_2SO_4$. Particle hygroscopic growth at sub-saturated conditions (g_i) is obtained by:

$$g(RH) = \frac{d_m(RH)}{d_p} \qquad (6)$$

where $d_m(RH)$ and d_p are the geometric mean mobility diameters of the sampled particles at the hydrated state (i.e. at RH=86%) as measured by DMA-2 and the CPC, and at the dry state selected by DMA-1 (RH< 30%), respectively. Particle size distributions at 86% RH were inverted using the TDMAfit algorithm (Stolzenburg and McMurry, 1988) which is also capable of distinguishing between internally and externally mixed aerosols (e.g. Bezantakos et al., 2013).

Hygroscopicities determined from the CCN measurements are differentiated by corresponding values from the HTDMA measurements by including and index CCN, HTDMA, respectively (e.g. κ_{HTDMA}, κ_{CCN}). κ_{HTDMA} is calculated from the HTDMA-measured sub-saturated hygroscopic growth factors using:

$$\kappa_{HTDMA} = (g(RH)^3 - 1)\left(\frac{\exp(\frac{A}{g(RH) * d_p})}{\frac{RH}{100\%}} - 1 \right) \qquad (7)$$

with A being the Kelvin paraeter defined in Equation 3. The exponential term of this equation (i.e. the Kelvin term) is used to account for curvature effects on vapor pressure.

An average value of the hygroscopic parameter at each dry particle size, d_p , which is representative of the hygroscopic properties of the entire particle population is obtained as follows:

$$\overline{\kappa_{HTDMA}} = \int_{g_{\min}}^{g_{\max}} \kappa(g_{(RH)}) p(g_{(RH)}) dg_{(RH)} \qquad (6)$$

where $\kappa(g_{(RH)})$ is obtained from the growth factor probability distribution using equation 5 and $p(g_{(RH)})$ is the probability of each growth factor. $g_{\min}$, $g_{\max}$ are the minimum and maximum growth factors, respectively, obtained from the growth factor probability distribution and represent the minimum and maximum g with non-zero probability value.

To support the *in situ* instruments, we used space-borne laser remote sensing (lidar) data from CALIOP (Mamouri et al., 2009; Winker et al., 2009) to characterize the plumes emerging from the fire hot spots. The fire plume originating from any location can be tracked by HYSPLIT back-trajectory analysis (Bougiatioti et al., 2014) and lidar observations can be used to check the presence of aerosol layers and aerosol types. Optical confirmation of the smoke plumes is provided by MODIS and FIRMS as shown in the supplementary material of Bougiatioti et al. 2014.

3. Results and Discussion

3.1 Identifying periods of biomass burning influence

Bougiatioti et al. (2014) identified the BB events analyzed here by the time evolution of absorption enhancements (BC) in the aerosol, which was further verified by FIRMS and back-trajectory analysis. During these events mass spectrometric biomass burning tracers (i.e. fragments m/z=60 and 73) also exhibited elevated levels. Clear biomass burning contribution was identified by source apportionment using Positive Matrix Factorization (PMF) analysis for four distinct events. The BB events considered include a severe fire event that burned most of the island of Chios (19–21 August), an extensive wildfire at the Dalmatian Coast in Croatia resulting in smoke plumes that spread across the Balkans during the period 28–30 August, and, less extensive fires on the Greek islands of Euboea (3-5 September) and Andros (12-13 September). All fire events exhibited discrete BBOA profiles depending on the biomass burning fuel, as presented in detail by Bougiatioti et al. (2014). Nevertheless, the organic aerosol derived from the aging of the biomass burning aerosol (OOA-BB) identified for all events had a similar profile, regardless of the BBOA it was derived from (Bougiatioti et al. 2014). Transport time estimate and backtrajectory analysis were conducted with the Plume Arrival (h) from Base Time graphics with the help of the HYSPLIT model (www.arl.noaa.gov/hysplit.php).MODIS and CALIOP measurements confirm the validity of the Bougiatioti et al. (2014) analysis, by clearly showing the origin, transport path and characteristics of the biomass burning plume from the Chios fire on 18 and 19 August 2012, respectively. Indeed, in Figure 2a we show the MODIS true color image showing the plume emerging from the Chios fires on 18 August 2012 as obtained during its 9.39 UTC overpass over Greece (Kyzirakos et al., 2014). The blue and red lines delineate the ground track of the CALIPSO satellite during its overpass over Crete several hours later on 19 August 2012 (the first between 00:27-00:40 and the second between11:34-11:47 UTC); the red star shows the sampling site at Finokalia station. The CALIPSO vertical profiles of the aerosol backscatter coefficient (in km^{-1}sr^{-1}) at 532 and 1064 nm for the two overpasses are shown in Figure 2b (left-hand side) together with the corresponding linear particle depolarization ratio at 532 nm obtained between 00:27:30-00:40 UTC (right-hand side). Comparing the midnight and the daytime aerosol backscatter profiles in Figure 2b, we observe that the midnight values are 3-4 times lower than the daytime ones for altitudes up to 3 km height. In addition, the daytime observations show a discrete aerosol layer below 1.5 km. As for the linear particle depolarization ratio it shows a mean value of 19% (up to 1.25 km height) and less than 6-10% (1.25-2 km).

Finally, we made use of the classification scheme of the CALIPSO data (Omar et al., 2009) to classify the different subtypes of aerosols in the plume captured during its first overpass over Crete on 19 August 2012 (00:27-00:40 UTC). This classification scheme, based on the optical and microphysical properties of the sampled aerosols indeed reveals the presence of a mixture of smoke, polluted dust and marine particles observed below a 3 km altitude (black color for smoke, brown for polluted dust and blue for marine) as shown in Figure 2c, within the depicted area between 39^{o}N, 24.1^{o}E-37^{o}N, 23.4^{o}E, just NW of the Finokalia station and along the CALIPSO ground track. According to this classification, over Crete the presence of polluted dust (mixed with smoke and marine aerosols) prevails within the marine boundary layer, which for Finokalia is approximately 1 km (Kalivitis et al., 2007), extending up to 0.8-1.2km height. This implies that for the 00:27–00:40 UTC time slot, the BB aerosols sampled by the ground-based in situ measurements at Finokalia would contribute less (due to dilution) to the global aerosol mass loading than, if measured, over the Western Crete.

3.2 PM$_1$ composition

The average mass concentration for the whole measurement period (mid-August to mid-November 2012), based on the ACSM measurements combined with BC from the aethalometer was 9.2±4.8 μg m^{-3}. The corresponding median concentrations for the main aerosol constituents were3.56, 1.31, 3.03 and 0.47 μg m^{-3} for sulfate, ammonium, organics and BC respectively. Figure 3 represents the time series of the major submicron species where it can be seen that during the fire events the contribution of organics and BC increased substantially (from 34.9 to 46.5% for organics and from 6.1 to 9.5% for BC) with a simultaneous reduction of that of sulfate. Source apportionment clearly shows that these increases are related to BB influences

(Bougiatioti et al. 2014). During all BB events there is a clear dominance of wood burning over fossil fuel contributions to BC. The wood burning component of BC is also provided as a reference, depicting the enhanced contribution of biomass burning during the highlighted events.

Based the size-resolved CCN activity measurements and the inferred hygroscopicity parameter κ of the aerosol (Equation 3), it is evident that the changes in the organics and sulfate mass fractions will also influence the CCN concentrations, activation fractions and hygroscopicity. As the ACSM provides bulk submicron chemical composition and thus, is not able to capture any sized-dependent chemical composition, the size-resolved CCN activity measurements are able to resolve distinct CCN activity and mixing state of the different particle sizes. These aspects are thoroughly investigated in the following sections.

3.3 CN and CCN number concentrations and biomass burning events

For all four events of biomass burning-influenced air masses arriving at Finokalia, the observed aerosol number concentration increased considerably, regardless of size. The increases are quantitatively expressed using averaged data from at least 6 hours prior to the arrival time of the BB smoke. For particle sizes above 100 nm, BB increased concentrations by 65% for the Chios fire, around 50% for the Croatia fire , 88% for the Euboea fire and about 150% for the Andros fire. Less pronounced increases was seen for the smaller particle sizes. The corresponding impacts on CCN concentrations for the classified aerosol are shown in Figure 4 for all fire events. Concentrations are given at the characteristic supersaturation, $s*$, of the monodisperse CCN as classified by DMA-1 (Section 2.2). Within each event, $s*$ did not vary by more than 13.6%; therefore most of the variability in CCN number can be attributed to variations in the size distribution, rather than shifts in the chemical composition (i.e., $s*$).

As expected, smaller particles exhibit a higher critical supersaturation (Bougiatioti et al., 2011). During periods with smoke influence, critical supersaturations tend to increase, indicating that particles associated with BB are less effective CCN compared to those of the background aerosol. . To quantify the direct influence of biomass burning to particle and CCN number concentrations we studied the concentration of the BBOA component, identified by PMF analysis of the ACSM mass spectra (Bougiatioti et al., 2014). The BBOA concentration time series depicts the arrival time of the smoke and the intensity of the BB influence.

The data shown in Figure 4 indicates that during the majority of the identified biomass burning events, CCN concentrations for the larger particles sizes increase, and follow the BBOA trend. This increase was more pronounced, depending on the proximity of the fire and therefore, the travel time of the air masses. Rose et al. (2010) also observed increases in CCN during a biomass burning event near the mega-city Guangzhou, China, where CCN number concentrations at s=0.068 and 0.27%, increased by 90 and 8%, respectively. The same study attributed these changes to increases in the particle size when BB influence was present.

Of all particle sizes examined, it appears that those having mobility diameter of 60 nm exhibit the least variability in terms of CCN number concentration before and during the BB influence (Figure 4, open circles). The concentrations however of the classified aerosol significantly increase during the BB event from Croatia (Figure 4b).This event, together with others of smaller extent, is associated with new particle formation (NFP) events. The observed frequency of NPF days at Finokalia is close to 30% (Kalivitis et al., 2015), regardless of the presence or not of BB-laden air masses. Based on aerosol chemical composition it appears that both gaseous sulfuric acid and organic compounds take part in the growth of nucleated particles to CCN-relevant sizes. These organic compounds that contribute to the nuclei growth may be of different origins including biogenic emissions, biomass burning and other possibly anthropogenic sources from long-range transport (Kalivitis et al. 2015). From Figure 4b it appears that when the BB event is combined with such an NPF event within a few hours, 60-nm particles are strongly influenced and their CCN concentrations increase considerably. The influence of BB to the hygroscopicity of 60-nm particles and the other sizes is examined in a subsequent section. A detailed discussion on these events and their contribution to CCN concentrations is provided by Kalivitis et al. (2015).

3.4 CCN activation fractions during fire events

As demonstrated in the preceding section, CCN number concentrations during the biomass burning events proportionately increased for the larger particle sizes. Figure 5 shows the activation fractions ($R_a(Q)$) for three of the four particle sizes and the four considered fire events(120 nm is not shown as it exhibits the same behavior as 100 nm). As an indicator of BB influence, we use the concentration of the aged BB factor identified in the ACSM spectra (OOA-BB), as it represents the atmospherically-processed component of BBOA. This factor is chosen as it constitutes a larger part of the organic aerosol (30%) with BB influence and whose ageing is expected to be reflected in terms of CCN activity.

For all particle sizes, the activation fractions are derived from the asymptote of the fitting to the sigmoidal function of the $R_a(s)$ during each supersaturation cycle and represents the CCN behavior at the highest supersaturations measured (s>0.6%). Figure 5 shows that even though CCN concentrations increase for particles larger than 80 nm, their activation fractions remain, more or less, stable and very close to unity throughout the events. This observation implies that almost all aerosol particles larger than 80 nm are CCN active at supersaturations higher than 0.6%, within uncertainties. This is not the case for 60 nm particles whose activation fractions at 0.6% s (and in the case of the Chios fire activation fractions of 80 nm particles as well at 0.4% s) exhibit the highest variability, with ratios approaching values as low as 40%. It can be seen that as concentrations of the OOA-BB start to increase, the activation fractions of 60 nm particles at ~0.6% s start to diminish. It thus appears, that larger particles are mostly internally mixed, as also seen by their high activation ratios, while small particles could be externally mixed populations. An indication of the heterogeneity of the smaller particle sizes compared to the larger ones is the slope of the sigmoid fit to the $Ra(s)$; the steeper the slope the more homogeneous the population and given that the 60 nm particles exhibited the broader slopes, the more heterogeneous these particles are. This can be explained by a size-dependent chemical composition and the presence of a population with notable lower hygroscopicity that prohibits the particles from acting as CCN and can be attributed to different sources and atmospheric processing (coagulation, cloud processing and condensation of secondary aerosol) that generally tend to internally mix the particles, rendering them more CCN active. Indeed, the lowest activation fractions occur for the strongest events where the time for transport and aging is most limited (hence least aged and hygroscopic). The particle chemical dispersion retrievals (Section 3.5) also supports this view. The same conclusion is also drawn from the data provided by Bougiatioti et al. (2011) for the same sampling site during summertime, and are verified by analysis of the chemical dispersion and HTDMA data shown in following sections. The evolution of the mixing state of each particle size is further investigated by the HTDMA measurements in a subsequent section (Section 3.6) as well.

3.5 Hygroscopicity and chemical heterogeneity during the biomass burning events

The characteristic hygroscopicity parameters, κ^*, derived from the CCN measurements for all particle sizes and for the four selected fire events are presented in Figure 6. As a reference for the arrival time and magnitude of the event, the concentration of the BBOA factor is also shown in the figure, which has the characteristics of the freshly-emitted BB aerosol and is expected to influence more the hygroscopicity of the particles. The smaller particles have the lowest κ_{CCN} values, and hygroscopicity consistently increased with size. This hygroscopicity trend has also been observed elsewhere (Dusek et al., 2010; Cerully et al., 2011; Levin et al., 2012; Paramonov et al., 2013; Liu et al., 2014), and is attributed to the enrichment in organic material of sub-100 nm particles. Based on the derived κ values for each particle size and with knowledge of the distinct species identified by the ACSM (organics, sulfate) and their respective hygroscopicities, the volume fractions for organics and inorganics (mainly ammonium sulfate) were estimated for each particle size. It occurs that indeed, 60 nm particles are, on average, 89% composed of organics while the respective values for 80, 100 and 120 nm particles are 70, 50 and 41%. Most of the accumulation mode particles result from condensation of secondary sulfates, nitrates and organics from the gas phase and coagulation of smaller particles (Seinfeld and Pandis, 2006). In order to examine the contribution of constituents from primary sources that are not measured by the ACSM to the accumulation mode particles, we compared the mass derived from the ACSM+BC and the integrated volume distribution from the SMPS converted to mass. During the examined fire events, the ACSM+BC was on average 68.6±19.3% of the SMPS-derived mass. Therefore this is an indication that non-refractory material neglected by the ACSM in the accumulation mode particles bears a small influence on particle hygroscopicity. Accumulation mode particles can also result from cloud processing and based on cloud droplet calculations presented in a subsequent section (Section 3.8) it appears that particles subject to atmospheric processing would be present in a separate mode are around 120 nm ($s_{\max}$ ~ 0.08%). Particles larger than 100 nm are usually more aged than the smaller particles and more immediately associated with BB plumes and the atmospheric processing they undergo (Kalivitis et al., 2015). The hygroscopicity parameter for 100 and 120 nm particles are very similar and the fact that the variability in the respective chemical composition is limited may indeed be attributed to cloud processing, while 80-nm particles are in between the lowest and highest κ_{CCN} values, an indication of size-dependent chemical composition of components with different hygroscopicities.

Figure 6 also shows that during the arrival of the biomass burning-laden air masses, κ values of all particle size ranges within 0.2-0.3. This observation is consistent with values observed from chamber experiments of fresh and aged biomass burning aerosol and in-situ studies from the field. Engelhart et al. (2012) performed a study where 12 different biomass fuels commonly burnt in North American wildfires were used to characterize their respective hygroscopicity. They found that while κ of freshly emitted BBOA prior to photochemical aging covered a range from 0.06 to 0.6, after a few hours of photochemical processing, the variability of biomass burning κ values from the different fuels was reduced and hygroscopicity converged to a value of 0.2±0.1 (Cerully et al., 2011; Engelhart et al., 2012). Based on the derived hygroscopicity parameters for each particles size before and during the BB influence it occurs that smoke causes a relative decrease of κ in the order of 22% for 80 nm particles, 30.6% for 100 nm particles and 30.9% for 120 nm particles on average for the four events while κ for 60 nm particles deviate by 14%.

During the fire events the contribution of organics and BC to the submicron aerosol mass fraction increased significantly while the presence of sulfate declined. This is expected to influence the CCN activity of the sampled aerosol particles as it would cause variations in the inorganic and organic mass fractions. It has already been established that as the organic mass fraction of aerosol increases, the κ value of primary aerosol decreases (Petters et al., 2009; Engelhart et al., 2012). With photochemical aging, the increased oxygenation of the freshly emitted BBOA may influence the hygroscopicity of the organic components, but the concurrent increase of the inorganic fraction of the aerosol contributes to the observed increase of κ_{CCN} (inorganic content vs aging).

To examine the impact of atmospheric processing and aging on the composition of the sampled aerosol, we studied the chemical dispersion $\sigma(\kappa)$ of the hygroscopicity parameter κ, expressed by the standard deviation of kappa around the most probable hygroscopicity κ^*, and its dependence on particle size. As normal operation uncertainties and the DMA transfer function can induce a broadening of $R_a(s)$ and $R_a(\kappa)$ and therefore contribute to $\sigma(\kappa)$, the inferred $\sigma(\kappa)$ contains a fairly constant instrument offset and a time-dependent constituent that is representative of the real chemical variability. This offset value, owing to the DMA transfer function and other instrument limits has been calculated to be roughly 0.25 (Cerully et al. 2011). Table 1 shows the calculated chemical dispersion, in terms of $\sigma(\kappa)/\kappa$, for the four fire events and the measured particle sizes. It is immediately apparent that the chemical dispersion is reduced with increasing particle size. 60-nm particles exhibit the highest dispersion especially for the Chios fire, suggesting that the smaller particles are a mixture of freshly-emitted BB particles and particles formed from the condensation of organics during the transport from the fire location to Finokalia, as by atmospheric processing organics become less volatile, increasing the chemical dispersion. The 80 and 100-nm particles from the Chios fire have high $\sigma(\kappa)/\kappa$ values while the ones from Euboea and Andros have considerably lower values, demonstrating the magnitude of the Chios fire and the degree of atmospheric processing that has taken place. Finally, 120-nm particles always have a low chemical dispersion, with $\sigma(\kappa)/\kappa$ values close to the instrument limit. Nevertheless, the chemical dispersion of all particle sizes appears to be influenced by the presence of BB as there is an average relative increase of $\sigma(\kappa)/\kappa$ values of 21, 28, 41 and 43% for 60, 80, 100 and 120 nm particles, respectively, before and during the event. The increased chemical dispersion of particles smaller than 80 nm can be, therefore, attributed to the heterogeneity of sources of these particles (which is also seen by CALIOP, Figure 3c) combined with lack of extensive cloud processing because the particles are too small to activate in boundary layer clouds in the region (Section 3.8). For larger particles, the chemical dispersion may be due to mixing with other types of aerosol that are not identified by the ACSM; microphysical processing such as condensational growth and cloud processing may be the reason why they exhibit a smaller chemical dispersion than smaller particles. Indeed, the surface area distributions (Figure S1 of the Supplement) peaks at around 200 nm which means that condensation of SOA mass is most effective in that size range. Coagulation/condensation continuously occurs together with any new source and NPF during atmospheric transport (Triantafyllou et al., 2016; Kalkavouras et al., in review), but cloud processing mixes everything and makes it completely homogeneous at the activation diameter that corresponds to each fire separately. In terms of aerosol microphysical processes, numerical simulations indicate that for half a day of aging under moderately polluted conditions, coagulation has been found to internally mix almost all particles above 0.2 μm, and smaller particles to a lesser extent (e.g. Jacobson, 2002). Condensation, for the same time scale, increases the fractional coating of small particles rather than large ones.

3.6 Particle growth factors during the fire events

From the concurrent HTDMA growth factor measurements at sub-saturated conditions we calculated the corresponding κ_{HTDMA} values. During the focus period of the biomass burning events as well as a few days before and after the events, the grand majority of the HTDMA data exhibited unimodal distributions, indicating that all selected particle fractions were internally mixed. Bimodal hygroscopicity distributions were only observed during the arrival of the smoke plumes from the most intense events and therefore are not taken into account for the comparison study between CFSTGC and HTDMA-derived κ values. Average CFSTGC-derived κ_{CCN} values and HTDMA-derived κ_{HTDMA} values for the selected particles sizes are given in Table 2. On average, κ_{HTDMA} values are somewhat lower than the respective κ_{CCN} values for the smaller particles, while the difference between them is larger for the larger particle sizes. Nevertheless, both time series follow the same trend and values are consistent within ±30% (κ_{HTDMA}=0.854 · κ_{CCN}, R^2=0.87; Figure S2 in the supplement). Owing to non-ideality in the aqueous phase, partial solubility of the organics and the existence of multiple phases under subsaturated conditions HTDMA-derived κ_{HTDMA} values may indeed be lower than the corresponding CCN-derived ones. In the study of Wu et al. (2013) κ derived from CCN measurements was also roughly 30% higher than that determined from hygroscopic growth measurements. Similar effects are also seen for laboratory generated aerosol composed of single and multiple compounds (Petters and Kreidenweis, 2007). Apart from non-ideality solution effects, the presence of surfactants produced during biomass burning events (Asa-Awuku et al., 2008) may also increase the discrepancies between κ-HTDMA and κ-CCN (Ruehl et al., 2012). Other studies as well note similar magnitude of difference between CFSTGC and HTDMA-derived κ values (e.g. Prenni et al., 2007; Massoli et al., 2010; Cerully et al. 2011).

The probability distribution of growth factors in the HTDMA give an independent measure of particle mixing state. During the two most intense fire events (i.e. during the Chios and Euboea fire) where the smoke plume had the least amount of transit and atmospheric processing time all sizes exhibited two different hygroscopic modes (Tables 3 and 4; Figure S3 in the supplement). These distinct modes were not observed during the other two events, owing to longer time of processing that allows for condensation growth and mixing of the populations. Figure 7 portrays in the left-hand panels the $\overline{\kappa_{HTDMA}}$ (estimated using Equation 6) for the sampled particle sizes during the Chios and Euboea fires. The right-hand panels show the respective particle size distributions obtained by the concurrent SMPS measurements, revealing the presence of different particle modes. It should be noted that values differ from the respective κ_{CCN} values, under subsaturated conditions, because if some particles do not grow inside the HTDMA they are directly assigned with a growth factor equal to one (i.e. κ=0), subsequently reducing considerably the derived kappa value. These hydrophobic particles are likely not fully counted by the CFSTGC and hence do not contribute to the average κ_{CCN}. During the arrival of the smoke-influenced air masses, there is a decrease in the hygroscopicity of all measured sizes. At the same time a bimodal distribution was observed by the SMPS (far right panels), indicative of two groups of particles, which can be partially due to the presence freshly emitted particles (i.e. smaller mode) in combination with larger, more processed ones. Adler et al. (2011) had also observed a shift in the average mode diameter of size distributions from 86±8nm for freshly-emitted BBOA to 114±7 nm for processed BBOA. This further supports the observed higher chemical dispersion in the smaller particle sizes(Section 3.5).

A similar behavior when the sampled particles influenced by biomass burning were exposed to sub-saturated conditions has been reported by Rissler et al. (2006). In those measurements the hygroscopic growth of the sampled particles when exposed at 90% RH showed that there was an external mixture of a nearly hydrophobic ($g_{(RH)}$=1.09 for 100 nm particles) and a moderately hygroscopic ($g_{(RH)}$=1.26) population. This reinforces our observations from the CCN measurements, where for super-saturated conditions, the activation fraction of mainly the 60 nm particles decreased significantly under influence of the smoke. A possible explanation why the activation fractions of the other size ranges remain close to unity during the smoke influence may be resulting from the cloud processing of these sizes and their mixing with background particles, contributing to their hygroscopicity and chemical dispersion. The overall characteristics are expected to be determined by the number fraction of the two modes in each size, combined with the occurrence of these two modes. If the presence of the bimodal samples is limited (less than 30%), then even though the fraction of the less hygroscopic mode may be as high as 45%, the overall activation fractions might not be influenced. For the first event (20-21/8) which was the most intense, the externally mixed samples represent almost 25% of the total sampled aerosol, with the occurrence of the bimodal samples increasing with increasing diameter (Table 3). It appears that in the bimodal samples the less hygroscopic mode initially dominates followed by a progressive dominance of the hygroscopic mode. It also appears that the increase in the less hygroscopic fraction coincides with the plume arrival time and the increase of the BBOA component, further supporting our findings of external mixing. During the second event (03-05/9) the bimodal samples increase, once more, with increasing diameter (5% for 60 nm to 28% for 120 nm particles). The less hygroscopic fraction in this case was dominant in approximately 33% of the samples, although this more hygroscopic mode had a κ_{HTDMA} value of 0.2 during the plume arrival time (Table 4). The more hygroscopic mode is therefore dominant in number for all sampled particles, which would explain that the activation fraction of the larger accumulation mode particles are not significantly affected by the presence of the less hygroscopic mode. On the other hand, the reason for the reduction of the activation fraction of 60-nm particles, apart from their hygroscopicity, can also be their different source and size, as during the events, the less hygroscopic mode is probably not activated, thus not detected by the CCN. This is not the case for the larger particles, as for example, 80-nm particles having a low κ_{HTDMA}=0.06 will still activate at the highest supersaturations sampled (s=0.67%).

3.7 Inferring size-dependent chemical composition and organic hygroscopicity

Assuming that the total aerosol hygroscopicity can be represented as the sum of the contribution of the different aerosol components:

$$\kappa = \sum_j \varepsilon_j \kappa_j \qquad (7)$$

where ε_j and κ_j are the volume fraction and hygroscopicity parameters of each species, respectively (Petters and Kreidenweis, 2007). With the use of this equation, and by assuming that the aerosol is a mixture of an organic and inorganic component, with the inorganic component being represented by ammonium sulfate, the total measured hygroscopicity, can be expressed by the sum:

$$\kappa = \varepsilon_{inorg}\kappa_{inorg} + \varepsilon_{org}\kappa_{org} \qquad (8)$$

Prior studies at Finokalia (Bougiatioti et al. 2009; 2011) have determined κ_{org}=0.158 and κ_{inorg}=0.6. Assuming this still applies and $\varepsilon_{inorg}+\varepsilon_{org}$=1, Equation 8 can be used to infer the volume fractions of organics and ammonium sulfate for the 4 different sizes, excluding the days of direct biomass burning influence. From this we obtain that 60 nm particles, on average, are composed of 82% organics and 18% ammonium sulfate; 80 nm particles of 44% organics and 55% ammonium sulfate, and, the larger particles contain a much larger fraction of ammonium sulfate (67% and 78% for 100 and 120 nm particles, respectively). This reinforces our conclusion based on the hygroscopicity measurements that the smaller particles are mostly composed of organic material.

These observations are in agreement with similar observations reported by Bezantakos et al. (2013) in the region of the Northern Aegean Sea.

The above approach can also be applied to the data from the fire events, as follows: we use only the larger size (120 nm) as from the former CCN studies in the area it was established that the hygroscopicity of the larger particles is close to the "bulk" hygroscopicity of the sampled aerosol (PM_1), which is constrained from the ACSM measurements (Bougiatioti et al., 2011). To evaluate the importance of the assumptions made in inferring the organic hygroscopicity from chemical composition, κ_{org} was additionally determined by applying Equation 8, for the 120 nm particles, where a set of κ equations is produced (n=228). Multivariable regression analysis within the excel environment is subsequently applied in order to determine the organic and inorganic component of the total hygroscopicity during the fire events. Based on the results, κ_{inorg}=0.61±0.03 and κ_{org}=0.137±0.02, values which are very similar to values determined by Bougiatioti et al. (2009; 2011). The confidence level is 95% and the resulting fit has an R^2=0.91 and p-values are smaller than $8\cdot10^{-7}$ for both components.

Taking the analysis one step further, we attempt a source apportionment of the organic hygroscopicity, by its attribution to different factors. Positive Matrix Factorization (PMF) analysis was applied to the time series of data from the direct influence from biomass burning. A detailed discussion of the PMF results can be found in Bougiatioti et al. (2014). During the focus period, 3 subtypes of organic aerosol (OA) were identified, namely biomass burning OA (BBOA), an OOA associated with biomass burning (OOA-BB) and a highly oxygenated OOA, having a relative contribution of 22, 32 and 46%, respectively. With the chemical composition measurements of the ACSM for the larger particle size (120 nm) combined with the respective κ_{CCN} we use the following equation to determine the hygroscopicity parameter of each factor:

$$\kappa = (1-\varepsilon_{org})\kappa_{inorg} + \varepsilon_{BBOA}\kappa_{BBOA} + \varepsilon_{OOA-BB}\kappa_{OOA-BB} + \varepsilon_{OOA}\kappa_{OOA} \tag{9}$$

Once again a set of 228 κ equations is produced and multivariable regression analysis is applied in order to deconvolve the organic hygroscopicity to its 3 subtypes. The confidence level once more is 95% and the resulting fit has an R^2=0.93, with p-values smaller than 0.001. It occurs that κ_{inorg}=0.62±0.04, κ_{BBOA}=0.057±0.07, κ_{OOA-BB}=0.138±0.11 and κ_{OOA}=0.169±0.09. As the occurrence of two modes of different hygroscopicity seen by the HTDMA during the arrival of the smoke coincide with the identification of BBOA by the ACSM, it is interesting to see that the inferred hygroscopicity for the freshly-emitted BBOA is very close to the hygroscopicity obtained by the HTDMA for the less hygroscopic component when two particle populations were present during the events (Tables 3 and 4, Section 3.6). When comparing the obtained hygroscopicity with the level of oxidation of each factor (O:C=0.2 for BBOA, 0.9 for OOA-BB and 1.2 for OOA; Bougiatioti et al., 2014) it occurs that the less hygroscopic component is also the least oxygenated and hygroscopicity increases with increasing O:C ratio. The calculated values are also comparable to the κ obtained by Chang et al. (2010) for the oxygenated organic component (OOA-1, OOA-2 and BBOA) of rural aerosol (κ_{ox}=0.22±0.04). They also found increased hygroscopicity with increasing ageing and degree of oxidation. Furthermore, the total organic hygroscopicity is very similar to that of the processed organic aerosol components, which make up almost 80% of the organic aerosol. Finally, based on the derived hygroscopicities for the BBOA and the processed BBOA (OOA-BB), it seems that the biomass burning organic aerosol becomes more hygroscopic, by almost a factor of two, with atmospheric processing.

Using the average diurnal profiles obtained from the PMF analysis combined with the corresponding mass fractions of each component and the inferred hygroscopicity parameter of each, we estimated the contribution of each factor to the overall κ_{org} and the total aerosol hygroscopicity. Figure 8 presents the resulting diurnal profiles from which it is clear that the grand majority of the organic hygroscopicity originates from the aged, very oxidized OOA. BBOA contributes around 7% to the organic hygroscopicity (2.2% to the overall aerosol hygroscopicity), which is small but not negligible, as it can be seen that when the BBOA contribution is the highest, there is an important decrease in the κ_{org}. Overall, organic aerosol associated with biomass burning can account for almost 35% of the organic hygroscopicity. By using the approach of Guo et al. (2015) where particle water is predicted using meteorological observations (relative humidity, temperature), aerosol composition and thermodynamic modeling (ISORROPIA-II; Fountoukis and Nenes, 2007), the LWC associated with the organic fraction is calculated. We find that although the freshly-emitted BBOA contributes merely 1.2% to the total organic water of the aerosol, the contribution of the processed OOA-BB is almost 33%. It is therefore clear that in the presence of biomass burning aerosol, both aerosol hygroscopicity but LWC as well may be influenced, thus affecting the overall direct and indirect aerosol radiative effects.

3.8 BB influence on droplet formation

The direct microphysical link between aerosol and clouds is the activation process, where a fraction of the aerosol contained within an ascending cloud parcel experiences unconstrained growth and activates to form cloud droplets. State of the art cloud droplet parameterizations (Ghan et al., 2011; Morales and Nenes, 2014) can accurately and rapidly calculate the droplet number (N_d) and maximum supersaturation (S_{max}) that would form in a cloud given knowledge of the aerosol distribution, composition and updraft velocity. Using the aerosol and hygroscopicity observations from all four BB events, we calculate the droplet number and supersaturation for clouds forming in the vicinity of Finokalia, using the droplet parameterizations based on the "population splitting concept" of Nenes and Seinfeld (2003), later improved by Barahona et al., (2010) and Morales and Nenes (2014). In the calculations of droplet number, the size distribution is represented by the sectional approach, derived directly from the SMPS distribution files. Values of updraft velocity are not known for Finokalia, but are obtained from the WRF regional model applied to late summer conditions (Tombrou et al., 2015); simulations suggest that the distribution of vertical velocities in the boundary layer around Finokalia display a spectral dispersion of σ_w = 0.2-0.3 m s^{-1} around a mean average value of 0.3. These values are generally consistent with vertical velocities observed in marine boundary layers (e.g., Ghate et al., 2011; Meskhidze et al., 2005). Given this, we can employ the characteristic velocity approach of Morales and Nenes (2010) when applying the droplet parameterization to obtain velocity PDF-averaged values of CDNC and S_{max}. As a sensitivity test, we also consider calculations for a convective boundary layer (σ_w = 0.6 ms^{-1}). The calculation of PDF-averaged values of CDNC and S_{max} is carried out for every distribution of aerosol number and composition measured for all four biomass burning events (5-min resolution distributions from the SMPS measurements for at least two days for each event). Results of all the calculations are shown in Figure 9. As a reference, the time series of the BBOA component is also portrayed.

For all events, the arrival of the smoke plume is followed by a considerable depression in the maximum supersaturation (relative average decrease 11.9±2.7% for σ_w = 0.3 ms^{-1} and 18±5.9% for σ_w = 0.6 ms^{-1}) that develops in clouds. This is a result of the enhanced competition for water vapor during cloud droplet formation for clouds affected by biomass burning smoke. The negative feedback of aerosol on supersaturation partially mitigates the observed increases in CCN to the point where clouds are highly insensitive to the large aerosol concentration increases (Moore et al., 2013; Zamora et al., 2016). As expected, increases in the updraft velocity (σ_w = 0.6 ms^{-1}) reduces the competition of CCN for water vapor, allowing S_{max} to increase, by almost 30%. The respective perturbation of N_d from BB influences by doubling the updraft velocity increases to 54% on average (from 9.3% to 24.2% for Chios, from 8.5% to 15.2% for Croatia, from 11% to 18.8% for Euboea and from 4% to 13.8% for Andros). The low supersaturations developed in BB-influenced clouds (here, as low as 0.06%) shifts the size of particles affected by cloud processing to the largest of particles (cutoff diameters before and during the Chios intense event were on average 133 and 109 nm, respectively while during the other events were on average 154.8 and 129.3 nm, respectively). Interestingly, the notable drop in chemical dispersion in the 100-120 nm particle sizes are consistent with the notion that cloud processing would considerably enhance their degree of internal mixing.

The degree to which BB influences N_d does not depend only on the value of updraft velocity and the intensity of the BB event; it also depends on the background aerosol. This is because the background preconditions the clouds and determines the levels of supersaturation that develops prior to the arrival of the BB aerosol. Highly polluted background generally means larger insensitivity of N_d to BB. This is shown clearly in Figure 10, which presents the droplet number concentration (top panel) and cloud maximum supersaturation (bottom panel) for each fire event as a function of BB influence, expressed by the sum of BBOA and OOA-BB ACSM factors. From the figure one can clearly see that when the background levels aerosol decreases (indicated by the lower N_d and higher S_{max} at the low end of BB factor concentrations, which is characteristic of the Coatia and Chios fires), N_d responds to increases in BB, up to the point where the clouds become “saturated” with aerosol (with a supersaturation around 0.08% and below, indicated by the shaded areas in Figure 10) and are insensitive to additional increases in BB. Euboea and Andros fires already have a high background, so the cloud droplet number is relatively insensitive to BB influence.

Finally, we estimated the relative contribution of chemical composition (from κ) and aerosol number concentration to the N_d, expressed by the average of the partial derivatives of dN_d/dN_a and dN_d/dN_κ and using the following equations:

$$\sigma^2 N_d = \sigma N_a \overline{\frac{\partial N_d}{\partial N_a}} + \sigma\kappa \overline{\frac{\partial N_d}{\partial N_\kappa}} \qquad (10)$$

where σ^2 is the variance of the droplet number (Nd), σNa is the standard deviation of the total aerosol number and $\sigma\kappa$ is the standard deviation of the hygroscopicity parameter. The relative contribution of each one of the total aerosol number (εN_a) and hygroscopicity parameter ($\varepsilon\kappa$) to the droplet number is estimated by:

$$\varepsilon\kappa_{Nd} = \sigma\kappa \frac{\overline{\frac{\partial N_d}{dN_\kappa}}}{\sigma^2 N_d} \qquad (11)$$

$$\varepsilon N_{aNd} = \sigma N_a \frac{\overline{\frac{\partial N_d}{\partial N_a}}}{\sigma^2 N_d} \qquad (12)$$

The results provided in Table 5 demonstrate that there are differences between the fire events, which can be attributed to the intensity of each event and thus the resulting concentrations, and the distance from the fire, thus the mixing and dilution during transport. The highest variance in N_d was calculated for the Andros event, which exhibited the lowest variability in $N_{aerosol}$ and the lowest variance was calculated for the Chios, followed by the Croatia event, which exhibited a variability in $N_{aerosol}$ of more than 1500 particles (cm^{-3}). From the relative contribution of the total aerosol number and chemical composition to N_d it can be seen that the closest the fire event is, the largest the contribution of aerosol number to the potential CDNC. As we move further away (e.g. Chios and Croatia) and the distance increases, the influence of the chemical composition becomes increasingly important, given the decrease of concentrations and dilution during transport.

4. Summary and Conclusions

This study provides CCN concentrations, subsaturated hygroscopicity, mixing state of size-selected aerosol particles and their impact on cloud formation in air masses influenced by summer biomass burning (BB) events in the eastern Mediterranean. The uniqueness of the dataset examined lies in nature of the fires, where smoke is mostly generated from isolated fires and subsequently transported and aged from a few hours to days before sampling. The presence of smoke in the most intense events is clearly identified by CALIPSO lidar remote sensing and the MODIS FIRMS product, while chemical markers and backtrajectory analysis confirm the influence of BB in every event. During each event, the contribution of organics and BC increased significantly while the concentration of sulfates decreased. This is shown to affect the hygroscopicity as well as the mixing state of the particles. The fire events had a direct influence on the total particle (CN) and CCN concentrations across all sizes; particle sizes larger than 100 nm exhibited an increase in absolute number of more than 50% and up to 30% for particles in the 60-80 nm range. The fraction of the smaller particles acting as CCN even at the highest level of measured supersaturation (0.6% s) however went significantly below unity in the presence of smoke. This and the overall value of hygroscopicity indicate that less CCN-active organic compounds are the dominant component of 60-nm and smaller particles (up to 82% of mass), while particles larger than 100 nm contain a much larger fraction of ammonium sulfate. The subsaturated hygroscopicity measurements confirms this, as 60-nm particles exhibited the lowest hygroscopic growth.

During the arrival of the biomass-burning-laden air masses, the average hygroscopicity parameters of all particle sizes converged to values between 0.2-0.3, which can be attributed to different chemical composition of all particles during these events, compared to background conditions. The hygroscopicity distributions and chemical dispersion analysis of the CCN data clearly show that smaller particles exhibit higher chemical diversity (variance in hygroscopicity equal to 0.15 κ units) than larger particles (variance in hygroscopicity less than 0.1 κ units) . This size-dependent mixing state may reflect the presence of different aerosol sources with characteristic sizes (e.g. sea-salt, pollution in addition to BB) and size-dependent chemical composition; the fact that smaller particles are less mixed than larger particles- together with that the background aerosol is composed of a large mode with a distinct chemical composition- suggests that the smaller particles are an external mixture of freshly emitted and secondarily formed particles that retain a large degree of mixing. Larger particles are further aged and subject to coagulation, condensation of secondary species and cloud processing, all of which tend to homogenize aerosol. . However, two aerosol populations with distinct hygroscopicity were seen were seen event at the largest sizes sampled during the most intense fire events. Nevertheless, their occurrence is limited and the overall activation of larger particles appears to be unaffected by the presence of these two populations. In terms of cloud processing effects, the largest particles that are predicted to form droplets in clouds in the vicinity of the sampling site indeed exhibit the lowest chemical dispersion. This supports the assumption of external mixing for smaller particles originating from biomass burning having decreased activation fractions and provides a plausible explanation of why larger particles appear, based on their activation fractions, not to be affected as far as their CCN-activity is concerned.

Using multivariable regression analysis and the volume fractions of organics and ammonium sulfate for the different particle sizes, we inferred the hygroscopicity of the organic fraction and found it equal to 0.115±0.017, which is consistent with published values from the literature. Using the results obtained from the source apportionment of the organic fraction we were able to deconvolve the organic hygroscopicity to its 3 subtypes. The hygroscopicity of freshly-emitted BBOA was found to be around 0.06, while the hygroscopicity of atmospherically-processed BBOA and highly oxidized organic aerosol was found to be 0.14 and 0.17, respectively. The inferred hygroscopicity of each component and its oxidation state are in line with the overall organic aerosol values observed. From this and the trends of each factor with atmospheric age we conclude that the organic fraction of biomass burning aerosol becomes more hygroscopic with atmospheric aging. Overall, organic aerosol associated with biomass burning (freshly emitted and processed) can account for 10% of the total aerosol hygroscopicity (2.2 and 7.6% for BBOA and OOA-BB, respectively). For the observed levels of relative humidity, and amount of each organic aerosol factor, we estimate that BBOA and OOA-BB contribute anywhere between 1.2 and 32.6% of the total organic water of the aerosol.

Towards understanding the impacts of the observed BB on clouds, we study the behavior of cloud droplet formation for typical boundary layer conditions. For this, we apply a state of the art cloud droplet formation parameterization to the observations, assuming typical values of updraft velocity for marine boundary layer clouds. We find that the very high concentrations of CCN during the influence of BB events tend to promote the competition for cloud water vapor, and substantially depresses the cloud supersaturation down to very low levels (even as low as 0.06%). As a result, only the largest of particles, from 110-150nm diameter and above, can activate to form cloud droplets. This also means that droplet number becomes highly insensitive to changes in aerosol in the presence of BB; indeed clouds influenced by BB exhibit a relative decrease in maximum supersaturation by 12% while at the same time, augments the potential droplet number by 8.5%. These results also support the chemical dispersion/mixing state analysis of the CCN data, as only the largest of aerosol sizes sampled activates and is exposed to cloud processing. Based on the average sensitivity of droplet number to changes in aerosol number and composition and observed variances thereof, we attribute the relative contribution of chemical composition and total aerosol number to the variance of droplet number. We find that the distance from the source is a key parameter that governs the importance of each parameter, with the influence of the chemical composition becoming increasingly important (controlling up to 25% of the droplet number variability) with growing distance from the source. Close to sources, the exclusive majority (98% and above) of the predicted droplet number variability is attributed to aerosol number variations. Therefore, although BB burning may strongly elevate CCN numbers, the relative impacts on cloud droplet number (compared to background levels) is eventually limited by water vapor availability and depends on the aerosol levels associated with the background.

Acknowledgments

The work of A. Bougiatioti, A. Papayannis, P. Kokkalis was supported by the “MACAVE” research project and the work of N. Kalivitis by the"FRONT" research project, which are implemented within the framework of the action Supporting of Postdoctoral Researchers of the Operational Program Education and Lifelong Learning (action’s beneficiary: General Secretariat for Research and Technology), and is co-financed by the European Social Fund (ESF) and the Greek State. This research has also been co-financed by the European Union (European Social Fund – ESF) and Greek national funds through the Operational Program "Education and Lifelong Learning" of the National Strategic Reference Framework (NSRF) - Research Funding Program: THALES, Investing in knowledge society through the European Social Fund. The financial support by the European Community through the ACTRIS Research Infrastructure Action and Bacchus project under the 7th Framework Programme (Grant Agreements no 262254 and 603445, respectively) are gratefully acknowledged. AN acknowledges support from a Georgia Power Faculty Scholar Chair and a Cullen-Peck Faculty Fellowship.

References

Adler, G., Flores, J.M., Abo Riziq, A., Borrmann, S., and Rudich, Y.: Chemical, physical, and optical evolution of biomass burning aerosols: a case study, Atmos. Chem. Phys., 11, 1491-1503, doi:10.5194/acp-11-1491-2011, 2011.

Andreae, M. O., Rosenfeld, D., Artaxo, P., Costa, A. A., Frank, G. P., Longo, K. M., and Silva Dias, M. A. F.: Smoking rain clouds over the Amazon, Science, 303, 1337–1342, 2004.

Asa-Awuku, A., Nenes, A., Sullivan, A.P., Hennigan, C.J. and Weber, R.J.: Investigation of molar volume and surfactant characteristics of water-soluble organic compounds in biomass burning aerosol, Atmos. Chem. Phys., 8, 799-812, 2008.

.Barahona, D., West, R.E.L., Stier, P., Romakkaniemi, S., Kokkola, H., and A. Nenes: Comprehensively Accounting for the Effect of Giant CCN in Cloud Activation Parameterizations, Atmos. Chem. Phys., 10, 2467-2473, 2010.

Bezantakos, S., K. Barmpounis, M. Giamarelou, E. Bossioli, M. Tombrou, N. Mihalopoulos, K. Eleftheriadis, J. Kalogiros, J.D. Allan, A. Bacak, C.J. Percival, H. Coe and G. Biskos: Chemical Composition and Hygroscopic Properties of Aerosol Particles over the Aegean Sea, Atmos. Chem. Phys., 13 (22), 11595–608, doi:10.5194/acp-13-11595-2013, 2013.

Biskos, G., D. Paulsen, L. M. Russell, P. R. Buseck, and S. T. Martin: Prompt Deliquescence and Efflorescence of Aerosol Nanoparticles, Atmos. Chem. Phys. 6, 4633–42, 2006.

Bougiatioti, A., Fountoukis, C., Kalivitis, N., Pandis, S.N., Nenes, A., and Mihalopoulos, N.: Cloud condensation nuclei measurements in the marine boundary layer of the eastern Mediterranean: CCN closure and droplet growth kinetics, Atmos. Chem. Phys., 9, 7053-7066, 2009.

Bougiatioti, A., Nenes, A., Fountoukis, C., Kalivitis, N., Pandis, S.N., and Mihalopoulos, N.: Size-resolved CCN distributions and activation kinetics of aged continental and marine aerosol, Atmos. Chem. Phys., 11, 8791-8808, doi:10.5194/acp-11-8791-2011, 2011.

Bougiatioti, A., Stavroulas, I., Kostenidou, E., Zarmpas, P., Theodosi, C., Kouvarakis, G., Canonaco, F., Prévôt, A.S.H., Nenes, A., Pandis, S.N., and Mihalopoulos, N.: Processing of biomass-burning aerosol in the eastern Mediterranean during summertime, Atmos. Chem. Phys., 14, 4793-4807, doi:10.5194/acp-14-4793-2014, 2014.

Carlton, A. G. and Turpin, B. J.: Particle partitioning potential of organic compounds is highest in the Eastern US and driven by anthropogenic water, Atmos. Chem. Phys., 13, 10203–10214, doi:10.5194/acp-13-10203-2013, 2013.

Cerully, K.M., Raatikainen, T., Lance, S., Tkacik, D., Tiitta, D., Petäjä, T., Ehn, M., Kulmala, M., Wornsop, D.R., Laaksonen, A., Smith, J.N. and Nenes, A.: Aerosol hygroscopicity and CCN activation kinetics in a boreal forest environment during the 2007 EUCAARI campaign, Atmos. Chem. Phys., 11, 12369-112386, doi:10.5194/acp-11-12369-2011, 2011.

Cerully, K. M., Bougiatioti, A., Hite Jr., J. R., Guo, H., Xu, L., Ng, N. L., Weber, R., and Nenes, A.: On the link between hygroscopicity, volatility, and oxidation state of ambient and water-soluble aerosol in the Southeastern United States, Atmos. Chem. Phys. Discuss., 14, 30835-30877, doi:10.5194/acpd-14-30835-2014, 2014.

Chang, R. Y-W., Slowik, J. G., Shantz, N. C., Vlasenko, A., Liggio, J.,Sjostedt, S. J., Leaitch, W. R., and Abbatt, J. P. D.: The hygroscopicity parameter (κ) of ambient organic aerosol at a field site subject to biogenic and anthropogenic influences: relationship to degree of aerosol oxidation, Atmos. Chem. Phys., 10, 5047−5064, doi:10.5194/acp-10-5047-2010, 2010.

Dusek, U., Frank, G. P., Curtius, J., Drewnick, F., Schneider, J., Kürten, A., Rose, D., Andreae, M. O., Borrmann, S., and Pöschl, U.: Enhanced organic mass fraction and decreased hygroscopicity of cloud condensation nuclei (CCN) during NPF events, Geophys. Res. Lett., 37, L03804, doi:10.1029/2009GL040930, 2010.

Engelhart, G. J., Hennigan, C. J., Miracolo, M. A., Robinson, A. L., and Pandis, S. N.: Cloud condensation nuclei activity of fresh primary and aged biomass burning aerosol, Atmos. Chem. Phys., 12, 7285-7293, doi:10.5194/acp-12-7285-2012, 2012.

Fountoukis, C. and Nenes, A.: ISORROPIA II: a computationally efficient thermodynamic equilibrium model for K^+-Ca^{2+}-Mg^{2+}-NH_4^+-SO_4^{2-}—NO_3^-—Cl^--H2O aerosols, Atmos. Chem. Phys., 7, 4639–4659, doi:10.5194/acp-7-4639-2007, 2007.

Fountoukis, C. and A. Nenes, A.: Continued Development of a Cloud Droplet Formation Parameterization for Global Climate Models, J.Geoph.Res.,110,D11212, doi:10.1029/2004JD005591, 2005.

Ghan, S.J., Abdul-Razzak, H., Nenes, A., Ming, Y., Liu, X., Ovchinnikov, M., Shipway, B., Meskhidze, N., Xu, J., Shi, X.: Droplet Nucleation: Physically-based Parameterization and Comparative Evaluation, J. Adv. Model. Earth Syst., 3, doi:10.1029/2011MS000074, 2011.

Ghate, V.P., Miller, M.A., and DiPretore, L.: Vertical velocity structure of marine boundary layer trade wind cumulus clouds, J. Geophys. Res., 116, D16, 2156-2202, doi:10.1029/2010JD015344, 2011.

Guo, H., Xu, L., Bougiatioti, A., Cerully, K.M., Capps, S.L., Hite, J.R.Jr., Carlton, A.G., Lee, S.-H., Bergin, M.H., Ng, N.L., Nenes, A., and Weber, R.J.: Fine-particle water and pH in the southeastern United States, Atmos. Chem. Phys., 15, 5211-5228, doi:10.5194/acp-15-5211-2015, 2015.

Healy, R.M., Riemer, N., Wenger, J.C., Murphy, M., West, M., Poulain, L., Wiedensohler, A., O'Connor, I.P., McGillicuddy, E., Sodeau, J.R., and Evans, G.E.: Single particle siversity and mixing state measurements, Atmos. Chem. Phys., 14, 6289-6299, doi:10.5194/acp-14-6289-2014, 2014.

Hildebrandt, L., Engelhart, G. J., Mohr, C., Kostenidou, E., Lanz, V. A., Bougiatioti, A., DeCarlo, P. F., Prevot, A. S. H., Baltensperger, U., Mihalopoulos, N., Donahue, N. M., and Pandis, S. N.: Aged organic aerosol in the Eastern Mediterranean: the Finokalia Aerosol Measurement Experiment – 2008, Atmos. Chem. Phys., 10, 4167 4186, doi:10.5194/acp-10-4167-2010, 2010.

Jacobson, M.Z.: Analysis of aerosol interactions with numerical techniques for solving coagulation, nucleation, condensation, dissolution, and reversible chemistry among multiple size distributions, J. Geophys. Res. Atmospheres, 107, D19, AAC 2-1-AAC 2-23, 2002.

Kalivitis, N., Gerasopoulos, E., Vrekoussis, M., Kouvarakis, G., Kubilay, N., Hatzianastassiou, N., Vardavas, I., and Mihalopoulos, N.: Dust transport over the eastern Mediterranean derived from Total Ozone Mapping Spectrometer, Aerosol Robotic Network, and surface measurements, J. Geophys. Res.-Atmos., 112, D03202, doi:10.1029/2006JD007510, 2007.

Kalivitis, N., Kerminen, V.-M., Kouvarakis, G., Stavroulas, I., Bougiatioti, A., Nenes, A., Manninen, H.E., Petäjä, T., Kulmala, M., and Mihalopoulos, N.: Atmospheric new particle formation as source of CCN in the Eastern Mediterranean marine boundary layer, Atmos. Chem. Phys. Discuss., 15, 11143-11178, doi:10.5194/acpd-15-11143-2015, 2015.

Kalkavouras, P., Bossioli, E., Bezantakos, S., Bougiatioti, A., Kalivitis, N., Stavroulas, I., Kouvarakis, G., Protonotariou, A.P., Dandou, A., Biskos, G., Nenes, A., Mihalopoulos, N., and Tombrou, M.: Regional variability of gaseous and particulate species and impacts on cloud formations at the South Aegean Sea during the Etesians, to be submitted to Atmos. Chem. Phys.

Kaufman, Y.J., and Remer, L.A.: Detection of forests using MID-IR reflectance-An application for aerosol studies, IEEE Trans. Geosci. Remote Sensing, 32 (3), 672-683, 1994.

Knutson, E.O., and Whitby, K.T.: Aerosol classification by electric mobility: Apparatus, theory, and applications, J. Aerosol Sci., 6, 443-451, 1975.

Kyzirakos, K., M. Karpathiotakis, G. Garbis, C. Nikolaou, K. Bereta, I. Papoutsis, T. Herekakis, D. Michail, M. Koubarakis, C. Kontoes, Wild fire monitoring using satellite images, ontologies and linked geospatial data, Web Semantics: Science, Services and Agents on the World Wide Web, 24, 18-26, 2014.

Lance, S.: Quantifying compositional impacts of ambient aerosol on cloud droplet formation, Published Doctoral Thesis, Available at http://etd.gatech.edu/theses/available/etd-11132007 175217/unrestricted/lance_sara_m_200712_phd[1].pdf, 2007.

Lance, S., Raatikainen, T., Onasch, T., Worsnop, D. R., Yu, X.-Y., Alexander, M. L., Stolzenburg, M. R., McMurry, P. H., Smith, J. N., and A. Nenes: Aerosol mixing-state, hygroscopic growth and cloud activation efficiency during MIRAGE 2006, Atmos. Chem. Phys., 13, 5049–5062, 2013.

Levin, E. J. T., Prenni, A. J., Petters, M. D., Kreidenweis, S. M., Sullivan, R. C., Atwood, S. A., Ortega, J., DeMott, P. J., and Smith, J. N.: An annual cycle of size-resolved aerosol hygroscopicity at a forested site in Colorado, J. Geophys. Res., 117, D06201, doi:10.1029/2011JD016854, 2012.

Liu, H. J., Zhao, C. S., Nekat, B., Ma, N., Wiedensohler, A., van Pinxteren, D., Spindler, G., Müller, K., and Herrmann, H.: Aerosol hygroscopicity derived from size-segregated chemical composition and its parameterization in the North China Plain, Atmos. Chem. Phys., 14, 2525−2539, doi:10.5194/acp-14-2525-2014, 2014.

Mamouri, R.E., V. Amiridis, A. Papayannis, E. Giannakaki, G. Tsaknakis, and D.S. Balis, Validation of CALIPSO space-borne derived aerosol vertical structures using a ground-based lidar in Athens, Greece, Atmos. Meas. Techn., 2, 513-522, 2009.

Mamouri, R.E., Papayannis, A., Amiridis, V., Müller, V., Kokkalis, P., Rapsomanikis, S., Karageorgos, E. T., Tsaknakis, G., Nenes, A., Kazadzis S., and Remoundaki, E.: Multi-wavelength Raman lidar, sunphotometric and aircraft measurements in combination with inversion models for the estimation of the aerosol optical and physico-chemical properties over Athens, Greece, Atmos. Meas. Tech., 5, 1793-1808, doi:10.5194/amt-5-1793-2012, 2012.

Massoli, P., Lambe, A. T., Ahern, A. T., Williams, L. R., Ehn, M., Mikkilä, J., Canagaratna, M.R., Brune, W. H., Onasch, T. B., Jayne, J. T., Petäjä, T., Kulmala, M., Laaksonen, A., Kolb, C.E., Davidovits, 5 P., and Worsnop, D. R.: Relationship between aerosol oxidation level and hygroscopic properties of laboratory generated secondary organic aerosol (SOA) particles, Geophys. Res. Lett., 37, L24801, doi:10.1029/2010GL045258, 2010.

Meskhidze, N., A. Nenes, Conant, W. C., and Seinfeld, J.H.: Evaluation of a new Cloud Droplet Activation Parameterization with In Situ Data from CRYSTAL-FACE and CSTRIPE, J. Geoph. Res., 110, D16202, doi:10.1029/2004JD005703, 2005.

Mihalopoulos, N., Stephanou, E., Kanakidou, M., Pilitsidis, S., and Bousquet, P.: Tropospheric aerosol ionic composition above the Eastern Mediterranean area, *Tellus*, **49B**, 314-326, 1997.

Moore, R.H. and Nenes, A.: Scanning Flow CCN Analysis - A Method for Fast Measurements of CCN Spectra, Aer.Sci.Tech., 43, 1192-1207, 2009.

Moore, R.H., Cerully, K., Bahreini, R., Brock, C.A., Middelbrook, A.M., and Nenes, A.: Hygroscopicity and composition of California CCN during summer 2010, J. Geophys. Res., 117, D00V12, doi:10.1029/2011JD017352, 2012a.

Moore, R.H., Raatikainen, T., Langridge, J.M., Bahreini, R., Brock, C.A., Holloway, J.S., Lack, D.A., Middlebrook, A.M., Perring, A.E., Schwarz, J.P., Spackman, J.R., and Nenes, A.: CCN spectra, hygroscopicity, and droplet activation kinetics of Secondary Organic Aerosol resulting from the 2010 Deepwater Horizon oil spill, Environ. Sci. Technol., 46, 3093-3100, 2012b.

Moore, R.H., Karydis, V.L., Capps, S.L., Lathem, T.L. and Nenes, A.: Droplet Number Prediction Uncertainties From CCN: An Integrated Assessment Using Observations and a Global Model Adjoint, Atmos. Chem. Phys., 13, 4235–4251, 2013.

Morales, R., and Nenes, A.: Characteristic updrafts for computing distribution-averaged cloud droplet number, autoconversion rate effective radius, J. Geophys. Res., 115, D18220, doi:10.1029/2009JD013233, 2010.

Morales Betancourt, R., and Nenes, A.: Aerosol Activation Parameterization: The population splitting concept revisited, Geosci. Mod. Dev., 7, 2345–2357, 2014.

Nenes, A. and Seinfeld, J.H.: Parameterization of cloud droplet formation in global climate models J.Geoph.Res, 108 (D7), 4415, doi: 10.1029/2002JD002911, 2003.

Ng, N. L., Herndon, S. C., Trimborn, A., Canagaratna, M. R., Croteau, P. L., Onasch, T. B., Sueper, D., Worsnop, D. R., Zhang, Q., Sun, Y. L., and Jayne, J. T.: An Aerosol Chemical Speciation Monitor (ACSM) for routine monitoring of the composition and mass concentration of ambient aerosol., Aerosol Sci. Tech., 45, 780–794, 2011.

Nguyen, T. B., Coggon, M. M., Flagan, R. C., and Seinfeld, J. H.: Reactive uptake and photo-Fenton oxidation of glycolaldehyde in aerosol liquid water, Environ. Sci. Technol., 47, 4307–4316, doi:10.1021/es400538j, 2013.

Omar, A. H., Winker, D. M., Kittaka, C., Vaughan, M. A., Liu, Z. Y., Hu, Y. X., Trepte, C. R., Rogers, R. R., Ferrare, R. A., Lee, K. P., Kuehn, R. E., and Hostetler, C. A.: The CALIPSO automated aerosol classification and lidar ratio selection algorithm, J. Atmos. Ocean. Tech., 26, 1994–2014, doi:10.1175/2009jtecha1231.1, 2009.

Paramonov M., P. P. Aalto, A. Asmi, N. Prisle, V.-M. Kerminen, M. Kulmala, and T. Petäjä, The analysis of size-segregated cloud condensation nuclei counter (CCNC) data and its implications for cloud droplet activation, Atmos. Chem. Phys., 13, 10285−10301, doi:10.5194/acp-13-10285-2013, 2013.

Petters, M.D., and Kreidenweis, S.M.: A single parameter representation of hygroscopic growth and cloud condensation nucleus activity, Atmos. Chem. Phys., 7, 1961-1971, doi: 10.5194/acp-8-6273-2008, 2007.

Petters, M.D., Wex, H., Carrico, C.M., Hallbauer, E., Massling, A., McMeeking, G.R., Poulain, L., Wu, Z., Kreidenweis, S.M., and Stratmann, F.: Towards closing the gap between hygroscopic growth and activation for secondary organic aerosol-Part 2: Theoretical approaches, Atmos. Chem. Phys., 9, 3999-4009, 2009.

Prenni, A.J., Petters, M.D., Kreidenweis, S.M., DeMott, P.J., and Ziemann, P.J.: Cloud droplet activation of secondary organic aerosol, J. Geophys. Res., 112, D10223, doi:10.1029/2006JD007963, 2007.

Rader, D.J., and McMurry P.H.: Application of the tandem differential mobility analyzer to studies of droplet growth or evaporation, J. Aerosol Sci., 17, 771-787, 1986.

Remy, S. and Kaiser, J. W.: Daily global fire radiative power fields estimation from one or two MODIS instruments, Atmos. Chem. Phys., 14, 13377-13390, doi:10.5194/acp-14-13377-2014, 2014.

Rissler, J., Vestin, A., Swietlicki, E., Fisch, G., Zhou, J., Artaxo, P., and Andreae, M.O.: Size distribution and hygroscopic properties of aerosol particles from dry-season biomass burning in Amazonia, Atmos. Chem. Phys., 6, 471-491, 2006.

Roberts, G., Nenes, A., Andreae, M.O., Seinfeld, J.H. (2003) Impact of Biomass Burning on Cloud Properties in the Amazon Basin, *J. Geophys. Res.*, **108**, doi: 10.1029/2001JD000985

Roberts, G.C., and Nenes, A.: A continuous-flow streamwise thermal-gradient CCN chamber for atmospheric measurements, Aerosol Sci. Technol., 39, 206-221, doi:10.1080/027868290913988, 2005.

Rose, D., Nowak, A., Achtert, P., Wiedensohler, A., Hu, M., Shao, M., Zhang, Y., Andreae, M. O., Poeschl, U.: Cloud condensation nuclei in polluted air and biomass burning smoke near the mega-city Guangzhou, China – Part 1: Size-resolved measurements and implications for the modeling of aerosol particle hygroscopicity and CCN activity, Atmos. Chem. Phys., 10, 3365–3383, doi:10.5194/acp-10-3365-2010, 2010.

Ruehl, C., Chuang, P.Y., Nenes, A., Cappa, C., and Kolesar, K.: New Evidence of Surface Tension Reduction in Microscopic Aqueous Droplets, Geoph. Res. Let., 39, L23801, doi:10.1029/2012GL053706, 2012.

Sandradewi, J., Prevot, A. S. H., Szidat, S., Perron, N., Lanz, V. A., Weingartner, E., and Baltensperger, U.: Using aerosol light absorption measurements for the quantitative determination of wood burning and traffic emission contributions to particulate matter, Environ. Sci. Technol., 42, 3316–3323, 2008.

Sciare, J., Bardouki, H., Moulin, C., Mihalopoulos, N.: Aerosol sources and their contribution to the chemical composition of aerosols in the Eastern Mediterranean Sea during summertime, Atmos. Chem. Phys., 3, 291–302, doi:10.5194/acp-3-291-2003, 2003.

Sciare, J., Oikonomou, K., Favez, O., Liakakou, E., Markaki, Z., Cachier, H., and Mihalopoulos, N.: Long-term measurements of carbonaceous aerosols in the Eastern Mediterranean: evidence of long-range transport of biomass burning, Atmos. Chem. Phys., 8, 5551-5563, 2008.

Seinfeld, J.H., and Pandis, S.N.: Atmospheric Chemistry and Physics: From Air Pollution to Climate Change, 2nd edition, J. Wiley, New York, 2006.

Spracklen, D.V., Carslaw, K.S., Pöschl, U., Rap, A., and Forster, P.M.: Global cloud condensation nuclei influenced by carbonaceous combustion aerosol, Atmos. Chem. Phys., 11, 9067-9087, doi:10.5194/acp-11-9067-2011, 2011.

Stolzenburg, M.R., and McMurry, P.H.: TDMAFIT User's Manual, Particle Technology Laboratory, Department of Mechanical Engineering, U of Minnesota, Minneapolis, MN 55455, 1988.

Stolzenburg, M.R. and McMurry, P.H.: An ultrafine aerosol Condensation Nucleus Counter, Aerosol Sci. Technol., 14, 48-65, 1991.

Tombrou, M., Bossioli, E., Kalogiros, J., Allan, J. D., Bacak, A., Biskos, G., Coe, H., Dandou, A., Kouvarakis, G., Mihalopoulos, N., Percival, C. J., Protonotariou, A. P. and Szabó-Takács, B.: Physical and chemical processes of air masses in the Aegean Sea during Etesians: Aegean-GAME airborne campaign, Sci. Total Environ., 506-507, 201–216, doi:10.1016/j.scitotenv.2014.10.098, 2015.

Triantafyllou, E., M. Giamarelou, E. Bossioli, P. Zarmpas, C. Theodosi, C. Matsoukas, M. Tombrou, N. Mihalopoulos, and G. Biskos: Particulate Pollution Transport Episodes from Eurasia to a Remote Region of Northeast Mediterranean, Atmos. Environ., 128, 45–52, doi:10.1016/j.atmosenv.2015.12.054, 2016.

Wiedensohler, A., Birmili, W., Nowak, A., Sonntag, A., Weinhold, K. et al.: Mobility particle size spectrometers: harmonization of technical standards and data structure to facilitate high quality long-term observations of atmospheric particle number size distributions, Atmos. Meas. Tech., 5, 657-685, 2012.

Winker, D. M., Vaughan, M. A., Omar, A., Hu, Y., Powell, K. A., Liu, Z., Hunt, W. H., and Young, S. A.: Overview of the CALIPSO mission and CALIOP data processing algorithms, J. Atmos. Ocean. Tech., 26, 2310–2323, doi:10.1175/2009JTECHA1281.1, 2009.

Zamora, L.M., Kahn, R.A., Anderson, B.E., Apel, E., Diskin, G.S., Jimenez, J.L., McFarquhar, G.M., Nenes, A., Wisthaler, A., Kondo, Y., Zelenyuk-Imre, A., and Ziemba, L.: Aircraft-measured indirect cloud effects from biomass burning smoke in the Arctic and subarctic, Atmos.Chem.Phys., 16, 715-738, 2016.

Table and Figure Captions

Table 1: Calculated chemical dispersion in terms of σ(κ)/κ for the four studied fire events and all measured particle sizes.

Table 2: Average CFSTGC-derived κ_{CCN} values and HTDMA-derived κ_{HTDMA} values for the selected particles sizes.

Table 3: Percentage of externally mixed samples (B_f), the hygroscopic parameter of the less and more hygroscopic mode (κ_1, κ_2), respectively, and the number fraction of particles residing in the less hygroscopic mode (N_{f1}) during the Chios event (20-21/08/2012).

Table 4: Same as Table 3, during the Euboea event (03-05/09/2012).

Table 5: Variance of N_d and relative contribution of aerosol number and chemical composition for the four fire events.

Figure 1: Schematic of the setup used for the CCN and mixing state measurements.

Figure 2: (a) Satellite composite view from MODIS of the fire plume emerging from the island of Chios on 18 August 2012 (courtesy on NASA). The blue and red lines delineate the two ground tracks of the CALIPSO satellite during its overpass over Crete on 19 August 2012 between 00:27-00:40 and 11:34-11:47 UTC, (b) Vertical profiles of the aerosol backscatter coefficient (in $km^{-1}sr^{-1}$) at 532 and 1064 nm (left) and linear particle depolarization ratio at 532 nm (right) measured by CALIPSO and (c) Vertical profiles of the aerosol subtypes captured by CALIPSO during its overpass over Crete; the marked area is located just at the NW of Finokalia station (00:27-00:40 UTC).

Figure 3: Time series concentrations of major PM_1 species that contribute in the identification of the BB events. The shaded areas represent the four considered fire events.

Figure 4: CCN concentrations for the selected particle sizes during the arrival of the smoke plumes for (a) Chios, (b) Croatia, (c) Euboea and (d) Andros. The black solid line represents the biomass burning component of the organic aerosol at the given time.

Figure 5: Activation fractions for the selected particle sizes during the arrival of the smoke plumes for (a) Chios, (b) Croatia, (c) Euboea and (d) Andros. The brown solid line represents the processed biomass burning component of the organic aerosol.

Figure 6: Characteristic hygroscopicity parameters of the selected particle sizes for (a) Chios, (b) Croatia, (c) Euboea and (d) Andros. The solid line represents the biomass burning component of the organic aerosol at the given time and circles represent the

smoke plume arrival time. The shaded areas represent the smoke plume influence period.

Figure 7: Hygroscopicity parameters derived from the HTDMA (a) & (c) and number size distributions from the SMPS (b) & (d) for the Chios and Euboea fire events, respectively. The shaded areas represent the smoke plume influence period.

Figure 8: Average diurnal contribution of each organic aerosol factor to the κ_{org} computed by multiplying the mass fraction by the corresponding inferred hygroscopicity parameter and the predicted diurnal profile of the total κ_{org} in the ambient aerosol.

Figure 9: Maximum supersaturation (S_{max}) (left panels) and potential droplet number (N_d) (right panels) for the four fire events of Chios (a,b), Croatia (c,d), Euboea (e,f) and Andros (g,h).

Figure 10: Droplet number concentration (top panel) and cloud maximum supersaturation (bottom panel) for each fire event as a function of BB influence, expressed by the sum of BBOA and OOA-BB ACSM factors.

Table 1

	60 nm	*80 nm*	*100 nm*	*120 nm*
Chios	0.85±0.14	0.73±0.14	0.60±0.20	0.41±0.16
Croatia	0.77±0.18	0.68±0.19	0.44±0.12	0.41±0.10
Euboea	0.70±0.20	0.49±0.10	0.32±0.08	0.29±0.06
Andros	0.71±0.10	0.52±0.13	0.34±0.10	0.30±0.06

Table 2

	κ_{HTDMA}	κ_{CCN}
60 nm	0.23±0.07	0.22±0.05
80 nm	0.28±0.1	0.39±0.1
100 nm	0.3±0.1	0.44±0.1
120 nm	0.33±0.11	0.49±0.13

Table 3

d_p (nm)	*Bf* (%)	κ_1	Nf_1	κ_2
60	6.9	0.05±0.02	0.17±0.06	0.18±0.01
80	20.0	0.05±0.02	0.33±0.14	0.19±0.03
100	23.0	0.06±0.03	0.43±0.24	0.21±0.04
120	30.4	0.05±0.03	0.47±0.19	0.2±0.04

Table 4

d_p (nm)	*Bf* (%)	κ_1	Nf_1	κ_2
60	5.3	0.09±0.07	0.37±0.34	0.31±0.19
80	15.2	0.06±0.04	0.31±0.17	0.2±0.03
100	26.5	0.05±0.03	0.39±0.19	0.19±0.03
120	28.2	0.05±0.03	0.40±0.19	0.19±0.03

Table 5

	$Variance N_d$		$Contribution\_\kappa$		$Contribution\_N_{aerosol}$	
	$w=0.3$	$w=0.6$	$w=0.3$	$w=0.6$	$w=0.3$	$w=0.6$
Chios	13.8	18.1	17.7%	12.6%	82.3%	87.4%
Croatia	34.4	47.7	26.7%	25.2%	73.3%	74.8%
Euboea	60.9	111.3	1.1%	2.2%	98.9%	97.8%
Andros	164.2	307.8	0.1%	0.15%	99.9%	99.8%

Figure 1

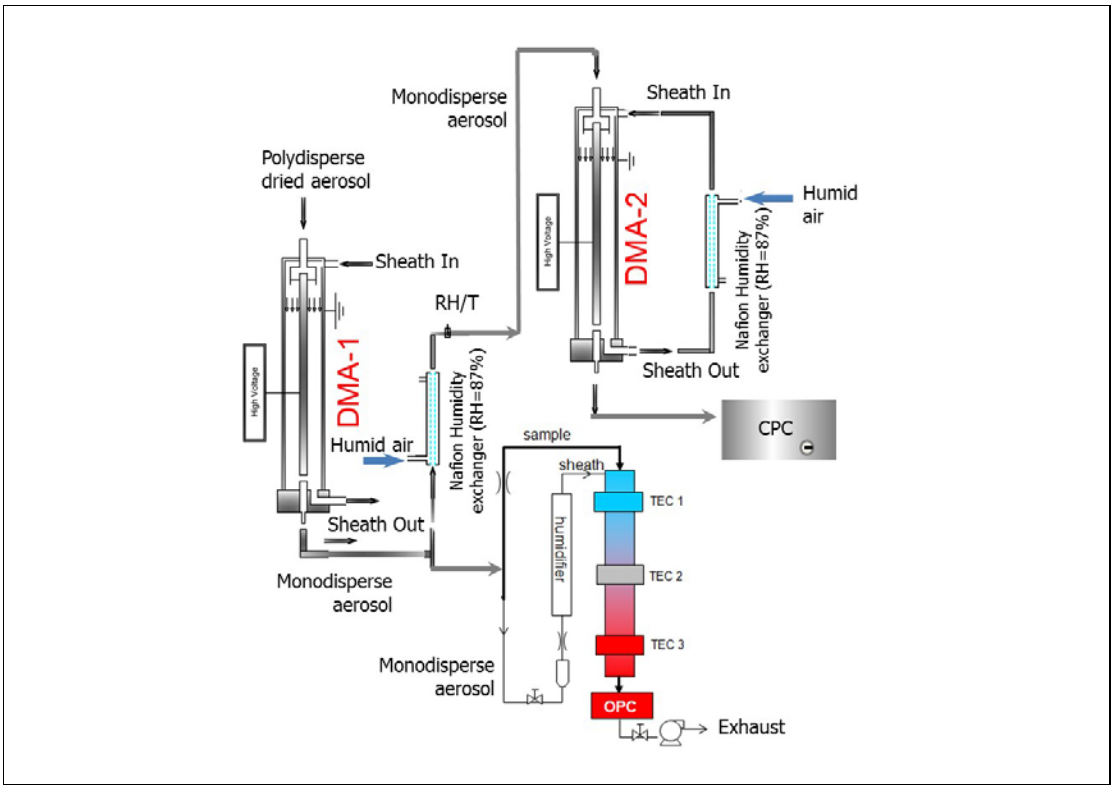
Monodisperse aerosol
Sheath In
Humid air
DMA-2
High Voltage
Nafion Humidity exchanger (RH=87%)
Sheath Out
Polydisperse dried aerosol
Sheath In
RH/T
DMA-1
High Voltage
Humid air
Nafion Humidity exchanger (RH=87%)
Sheath Out
CPC
sample
sheath
humidifier
TEC 1
TEC 2
TEC 3
Monodisperse aerosol
Monodisperse aerosol
OPC
Exhaust

Figure 2

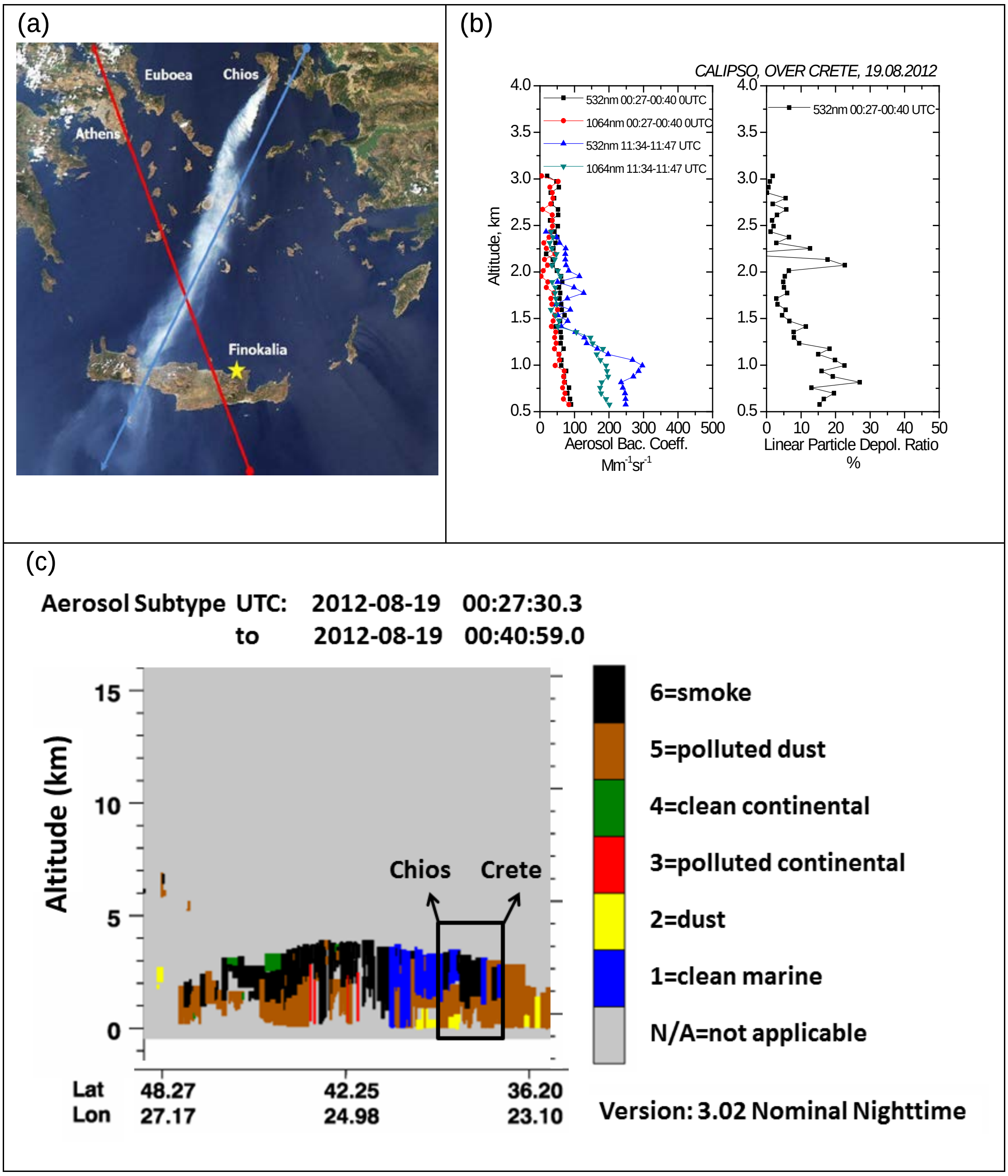
(a)
Euboea
Chios
Athens
Finokalia
(b)
CALIPSO, OVER CRETE, 19.08.2012
532nm 00:27-00:40 0UTC
1064nm 00:27-00:40 0UTC
532nm 11:34-11:47 UTC
1064nm 11:34-11:47 UTC
Altitude, km
4.0
3.5
3.0
2.5
2.0
1.5
1.0
0.5
0 100 200 300 400 500
Aerosol Bac. Coeff.
Mm-1sr-1
532nm 00:27-00:40 UTC
0 10 20 30 40 50
Linear Particle Depol. Ratio
%
(c)
Aerosol Subtype UTC: 2012-08-19 00:27:30.3
to 2012-08-19 00:40:59.0
Altitude (km)
15
10
5
0
Chios
Crete
Lat 48.27 42.25 36.20
Lon 27.17 24.98 23.10
6=smoke
5=polluted dust
4=clean continental
3=polluted continental
2=dust
1=clean marine
N/A=not applicable
Version: 3.02 Nominal Nighttime

Figure 3

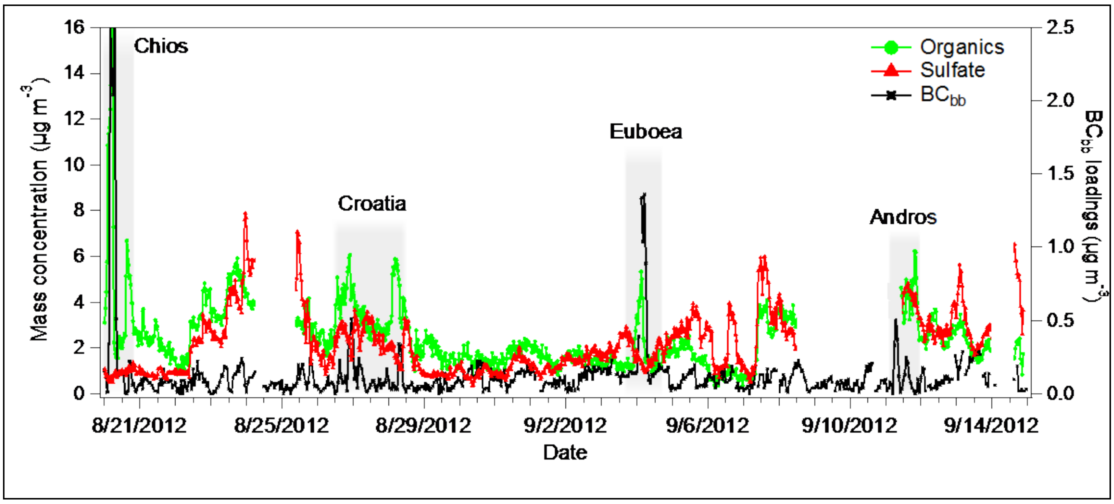
Chios
Croatia
Euboea
Andros
Organics
Sulfate
BC$_{bb}$
Mass concentration (μg m^{-3})
BC$_{bb}$ loadings (μg m^{-3})
16
14
12
10
8
6
4
2
0
2.5
2.0
1.5
1.0
0.5
0.0
8/21/2012
8/25/2012
8/29/2012
9/2/2012
9/6/2012
9/10/2012
9/14/2012
Date

Figure 4

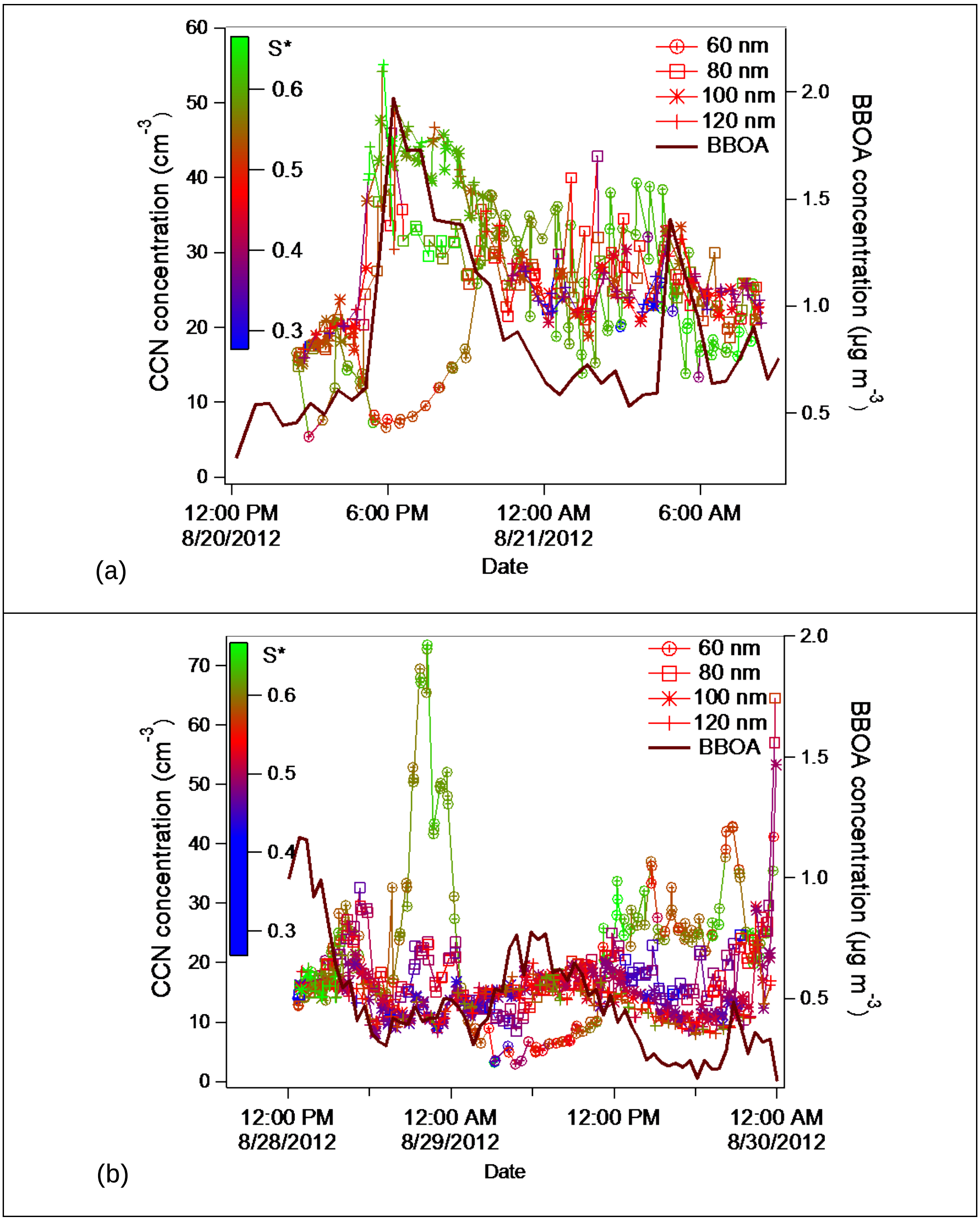
S*
0.6
0.5
0.4
0.3
60 nm
80 nm
100 nm
120 nm
BBOA
CCN concentration (cm^{-3})
BBOA concentration (µg m^{-3})
0
10
20
30
40
50
60
0.5
1.0
1.5
2.0
12:00 PM 8/20/2012
6:00 PM
12:00 AM 8/21/2012
6:00 AM
Date
(a)
S*
0.6
0.5
0.4
0.3
60 nm
80 nm
100 nm
120 nm
BBOA
CCN concentration (cm^{-3})
BBOA concentration (µg m^{-3})
0
10
20
30
40
50
60
70
0.5
1.0
1.5
2.0
12:00 PM 8/28/2012
12:00 AM 8/29/2012
12:00 PM
12:00 AM 8/30/2012
Date
(b)

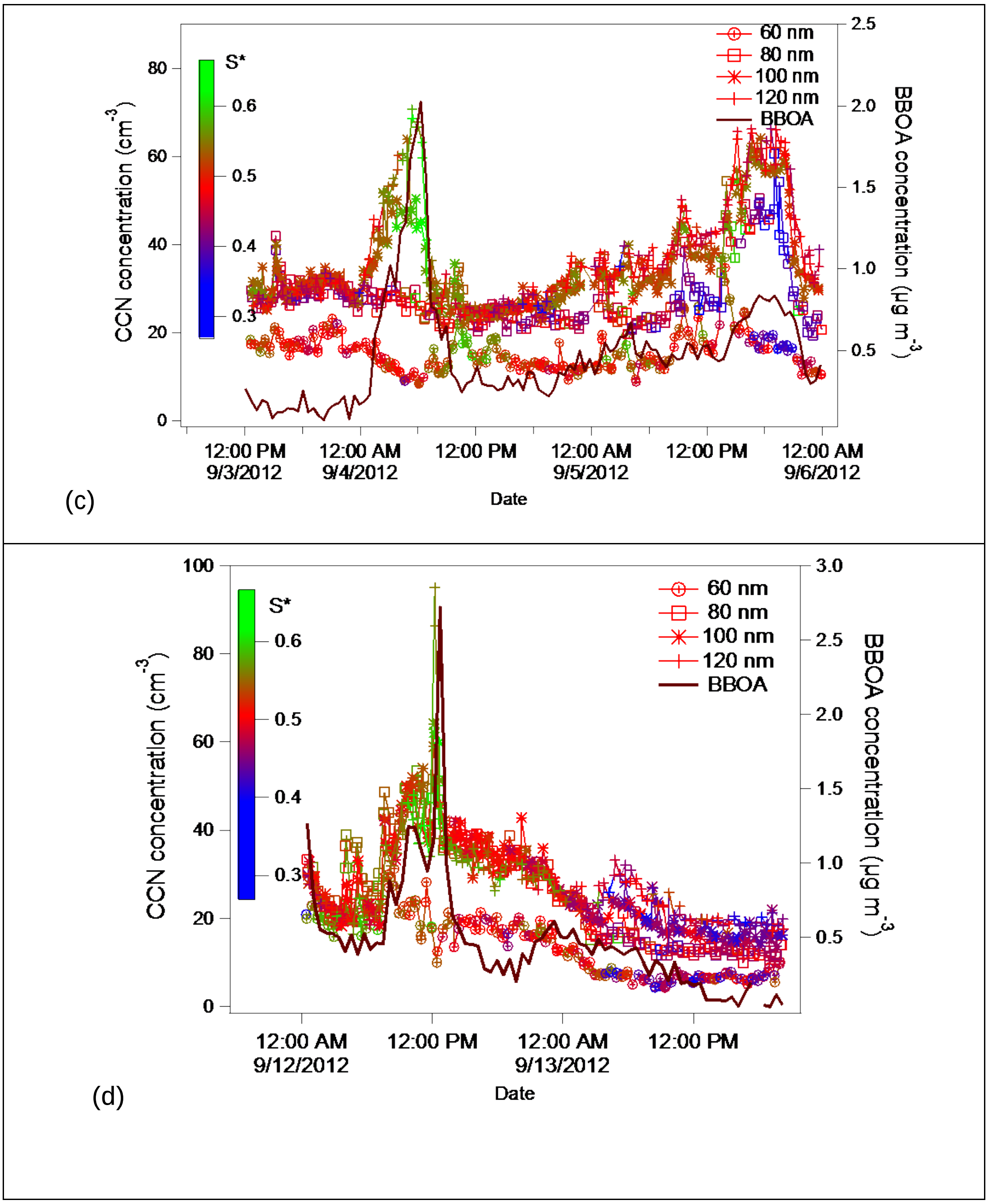
CCN concentration (cm^{-3})
BBOA concentration ($\mu g\ m^{-3}$)
S*
0.3
0.4
0.5
0.6
60 nm
80 nm
100 nm
120 nm
BBOA
0
20
40
60
80
0.5
1.0
1.5
2.0
2.5
12:00 PM 9/3/2012
12:00 AM 9/4/2012
12:00 PM
12:00 AM 9/5/2012
12:00 PM
12:00 AM 9/6/2012
Date
(c)
CCN concentration (cm^{-3})
BBOA concentration ($\mu g\ m^{-3}$)
S*
0.3
0.4
0.5
0.6
60 nm
80 nm
100 nm
120 nm
BBOA
0
20
40
60
80
100
0.5
1.0
1.5
2.0
2.5
3.0
12:00 AM 9/12/2012
12:00 PM
12:00 AM 9/13/2012
12:00 PM
Date
(d)

Figure 5

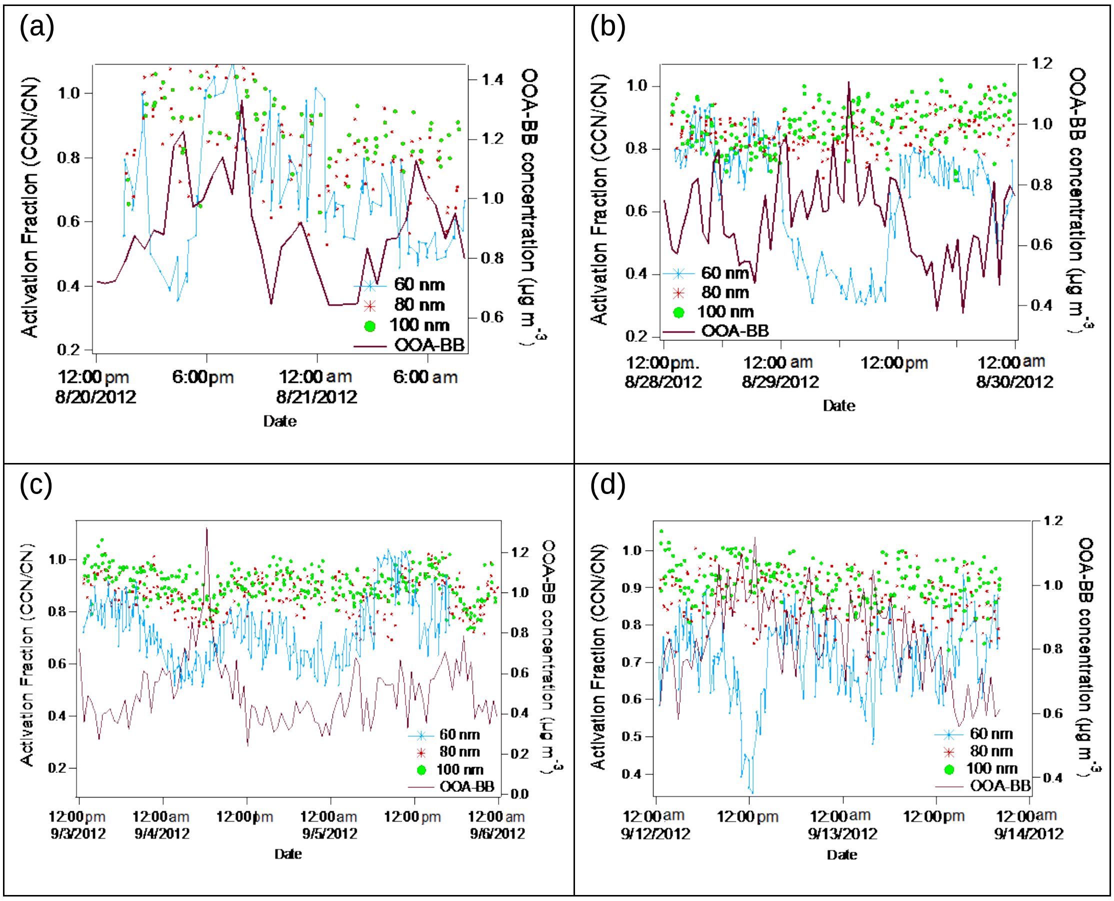
(a)
Activation Fraction (CCN/CN)
OOA-BB concentration (μg m^{-3})
60 nm
80 nm
100 nm
OOA-BB
12:00 pm 8/20/2012
6:00pm
12:00 am 8/21/2012
6:00 am
Date
(b)
Activation Fraction (CCN/CN)
OOA-BB concentration (μg m^{-3})
60 nm
80 nm
100 nm
OOA-BB
12:00pm. 8/28/2012
12:00 am 8/29/2012
12:00pm
12:00am 8/30/2012
Date
(c)
Activation Fraction (CCN/CN)
OOA-BB concentration (μg m^{-3})
60 nm
80 nm
100 nm
OOA-BB
12:00pm 9/3/2012
12:00am 9/4/2012
12:00pm
12:00am 9/5/2012
12:00pm
12:00am 9/6/2012
Date
(d)
Activation Fraction (CCN/CN)
OOA-BB concentration (μg m^{-3})
60 nm
80 nm
100 nm
OOA-BB
12:00am 9/12/2012
12:00pm
12:00am 9/13/2012
12:00pm
12:00am 9/14/2012
Date

Figure 6

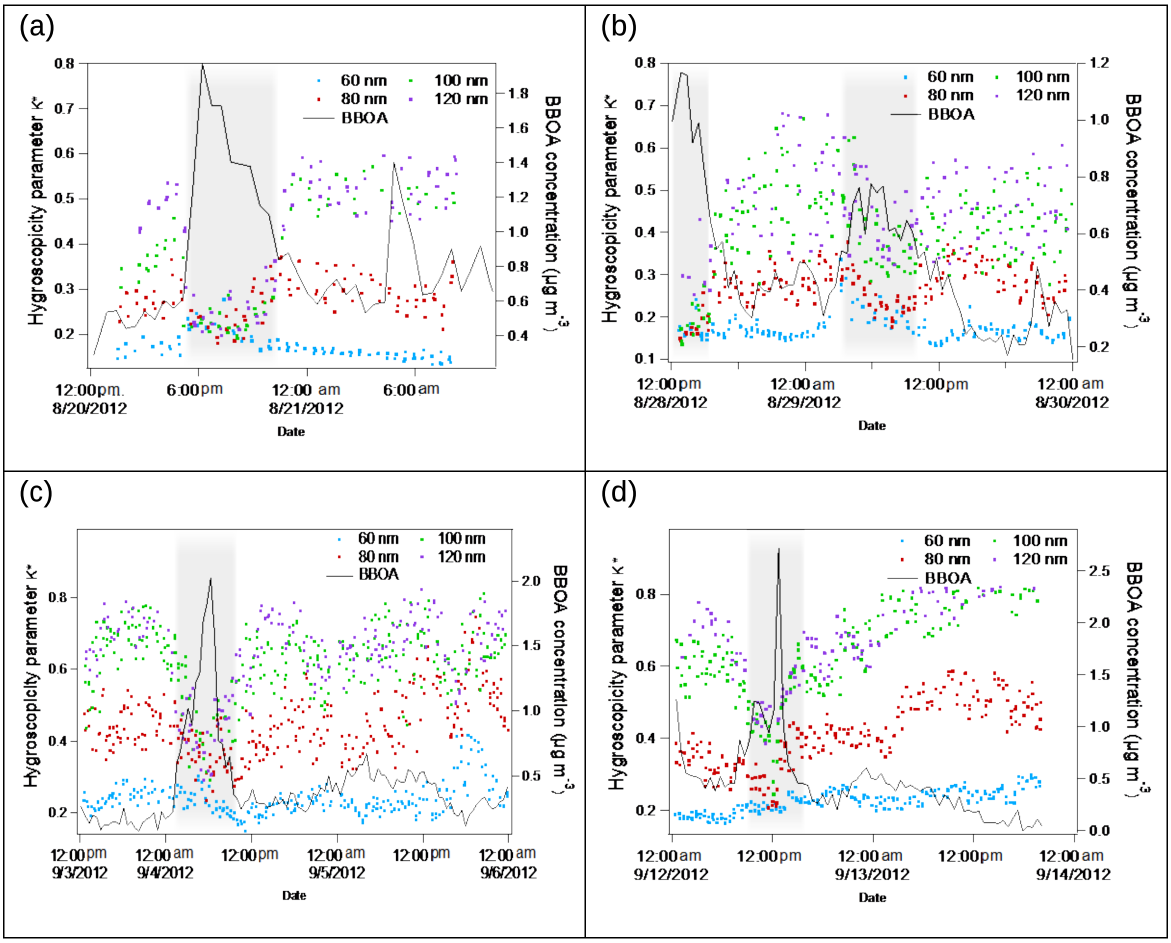
(a)
Hygroscopicity parameter κ*
BBOA concentration (μg m⁻³)
60 nm
80 nm
100 nm
120 nm
BBOA
0.8
0.7
0.6
0.5
0.4
0.3
0.2
1.8
1.6
1.4
1.2
1.0
0.8
0.6
0.4
12:00pm. 8/20/2012
6:00pm
12:00 am 8/21/2012
6:00am
Date
(b)
Hygroscopicity parameter κ*
BBOA concentration (μg m⁻³)
60 nm
80 nm
100 nm
120 nm
BBOA
0.8
0.7
0.6
0.5
0.4
0.3
0.2
0.1
1.2
1.0
0.8
0.6
0.4
0.2
12:00pm 8/28/2012
12:00am 8/29/2012
12:00pm
12:00 am 8/30/2012
Date
(c)
Hygroscopicity parameter κ*
BBOA concentration (μg m⁻³)
60 nm
80 nm
100 nm
120 nm
BBOA
0.8
0.6
0.4
0.2
2.0
1.5
1.0
0.5
12:00pm 9/3/2012
12:00am 9/4/2012
12:00pm
12:00am 9/5/2012
12:00pm
12:00am 9/6/2012
Date
(d)
Hygroscopicity parameter κ*
BBOA concentration (μg m⁻³)
60 nm
80 nm
100 nm
120 nm
BBOA
0.8
0.6
0.4
0.2
2.5
2.0
1.5
1.0
0.5
0.0
12:00am 9/12/2012
12:00pm
12:00am 9/13/2012
12:00pm
12:00am 9/14/2012
Date

Figure 7

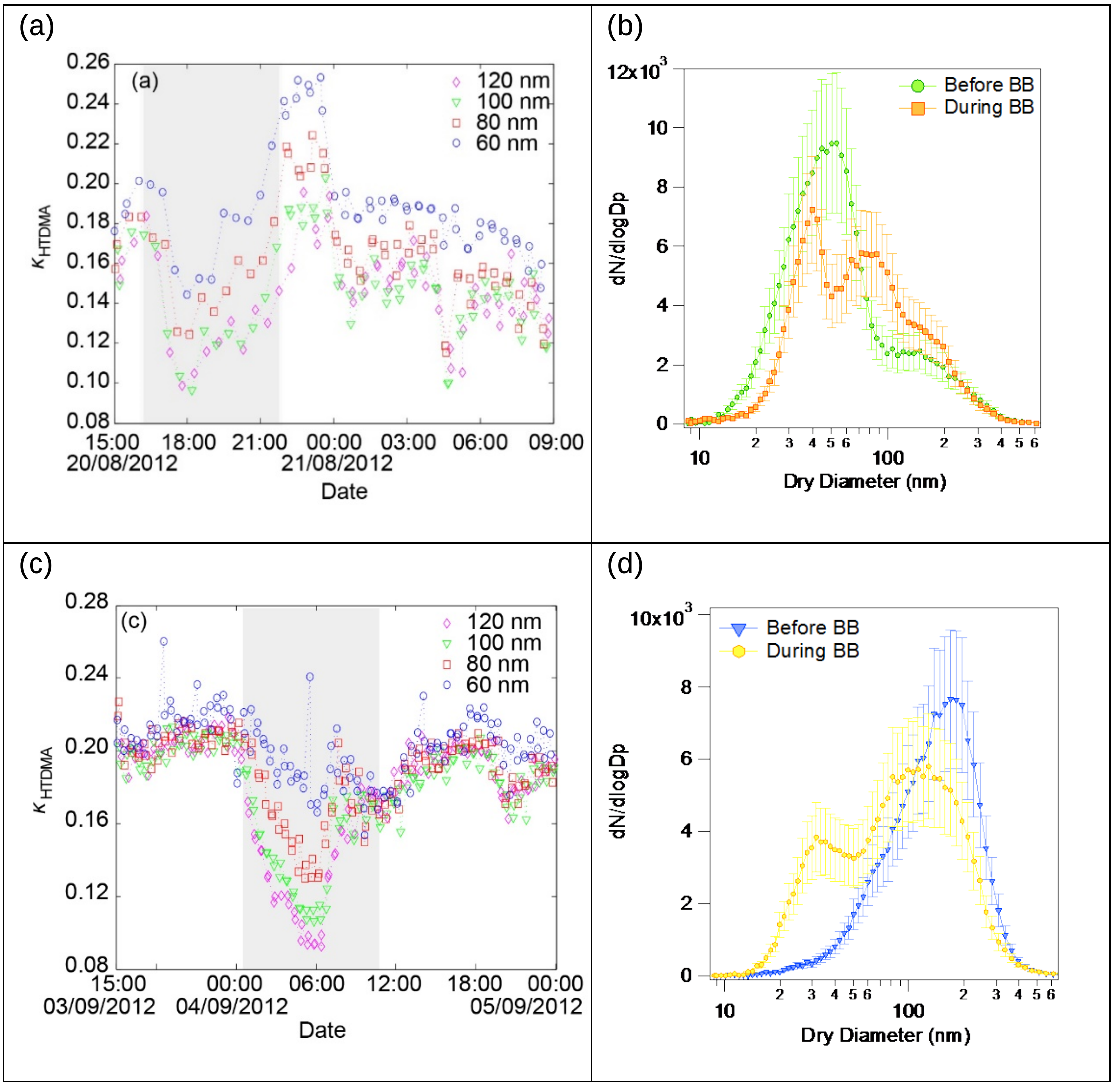
(a)
(a)
0.26
0.24
0.22
0.20
0.18
0.16
0.14
0.12
0.10
0.08
κ HTDMA
120 nm
100 nm
80 nm
60 nm
15:00
18:00
21:00
00:00
03:00
06:00
09:00
20/08/2012
21/08/2012
Date
(b)
12x10^3
10
8
6
4
2
0
dN/dlogDp
Before BB
During BB
10
100
2
3
4
5
6
Dry Diameter (nm)
(c)
(c)
0.28
0.24
0.20
0.16
0.12
0.08
κ HTDMA
120 nm
100 nm
80 nm
60 nm
15:00
00:00
06:00
12:00
18:00
00:00
03/09/2012
04/09/2012
05/09/2012
Date
(d)
10x10^3
8
6
4
2
0
dN/dlogDp
Before BB
During BB
10
100
Dry Diameter (nm)

Figure 8

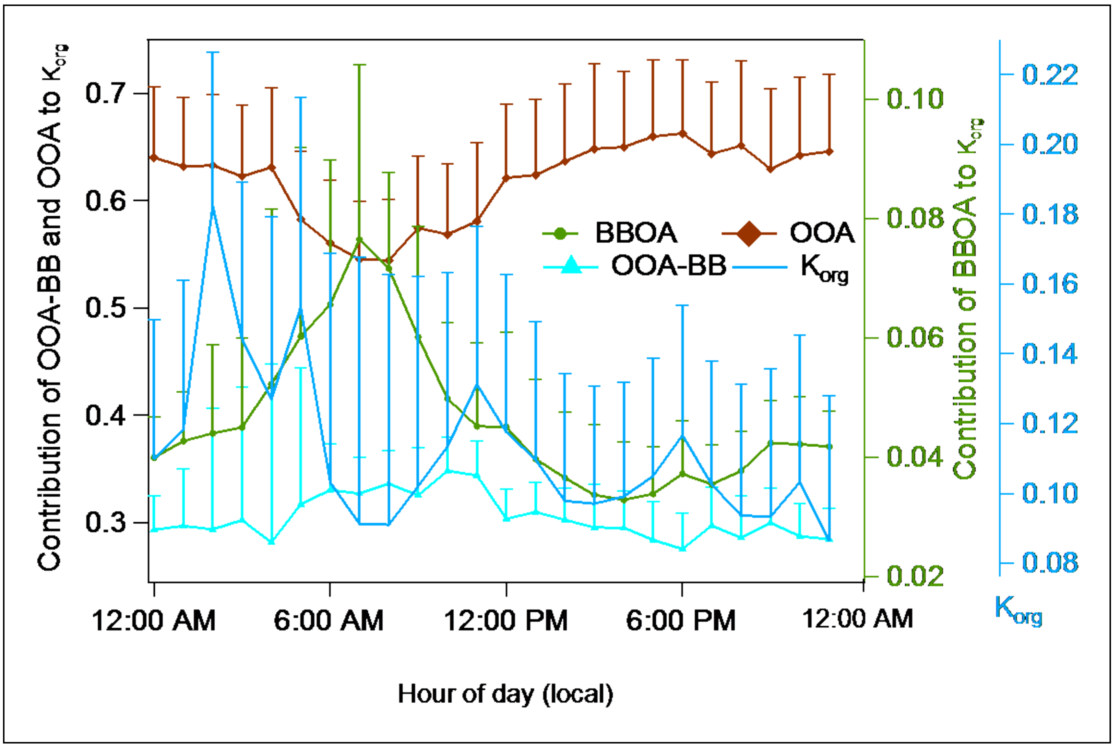
Contribution of OOA-BB and OOA to K_{org}
0.7
0.6
0.5
0.4
0.3
BBOA
OOA
OOA-BB
K_{org}
0.10
0.08
0.06
0.04
0.02
Contribution of BBOA to K_{org}
0.22
0.20
0.18
0.16
0.14
0.12
0.10
0.08
K_{org}
12:00 AM
6:00 AM
12:00 PM
6:00 PM
12:00 AM
Hour of day (local)

Figure 9

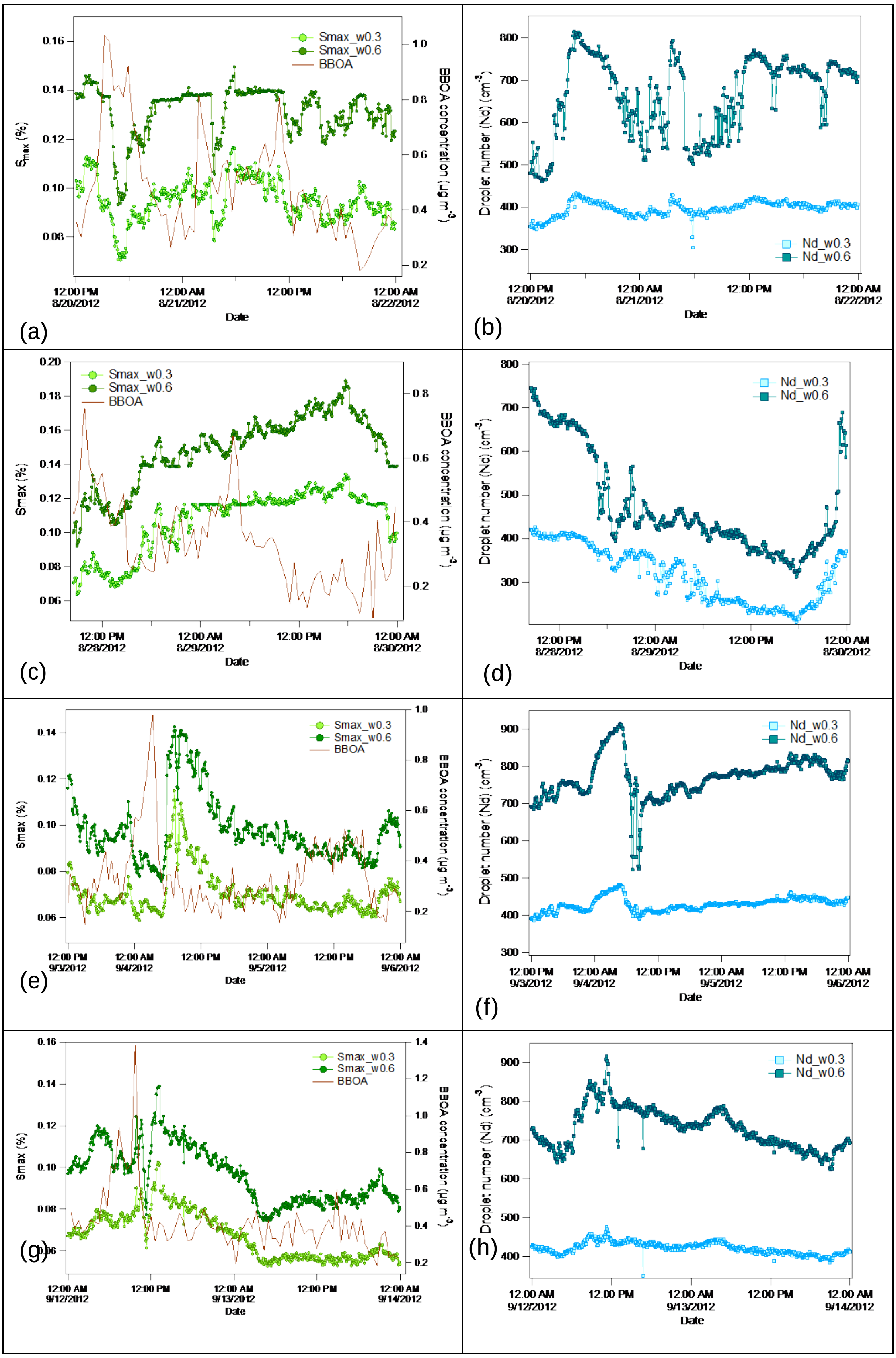
(a)
Smax (%)
Smax_w0.3
Smax_w0.6
BBOA
BBOA concentration (μg m-3)
12:00 PM 8/20/2012
12:00 AM 8/21/2012
12:00 PM
12:00 AM 8/22/2012
Date
(b)
Droplet number (Nd) (cm-3)
Nd_w0.3
Nd_w0.6
12:00 PM 8/20/2012
12:00 AM 8/21/2012
12:00 PM
12:00 AM 8/22/2012
Date
(c)
Smax (%)
Smax_w0.3
Smax_w0.6
BBOA
BBOA concentration (μg m-3)
12:00 PM 8/28/2012
12:00 AM 8/29/2012
12:00 PM
12:00 AM 8/30/2012
Date
(d)
Droplet number (Nd) (cm-3)
Nd_w0.3
Nd_w0.6
12:00 PM 8/28/2012
12:00 AM 8/29/2012
12:00 PM
12:00 AM 8/30/2012
Date
(e)
Smax (%)
Smax_w0.3
Smax_w0.6
BBOA
BBOA concentration (μg m-3)
12:00 PM 9/3/2012
12:00 AM 9/4/2012
12:00 PM
12:00 AM 9/5/2012
12:00 PM
12:00 AM 9/6/2012
Date
(f)
Droplet number (Nd) (cm-3)
Nd_w0.3
Nd_w0.6
12:00 PM 9/3/2012
12:00 AM 9/4/2012
12:00 PM
12:00 AM 9/5/2012
12:00 PM
12:00 AM 9/6/2012
Date
(g)
Smax (%)
Smax_w0.3
Smax_w0.6
BBOA
BBOA concentration (μg m-3)
12:00 AM 9/12/2012
12:00 PM
12:00 AM 9/13/2012
12:00 PM
12:00 AM 9/14/2012
Date
(h)
Droplet number (Nd) (cm-3)
Nd_w0.3
Nd_w0.6
12:00 AM 9/12/2012
12:00 PM
12:00 AM 9/13/2012
12:00 PM
12:00 AM 9/14/2012
Date

Figure 10

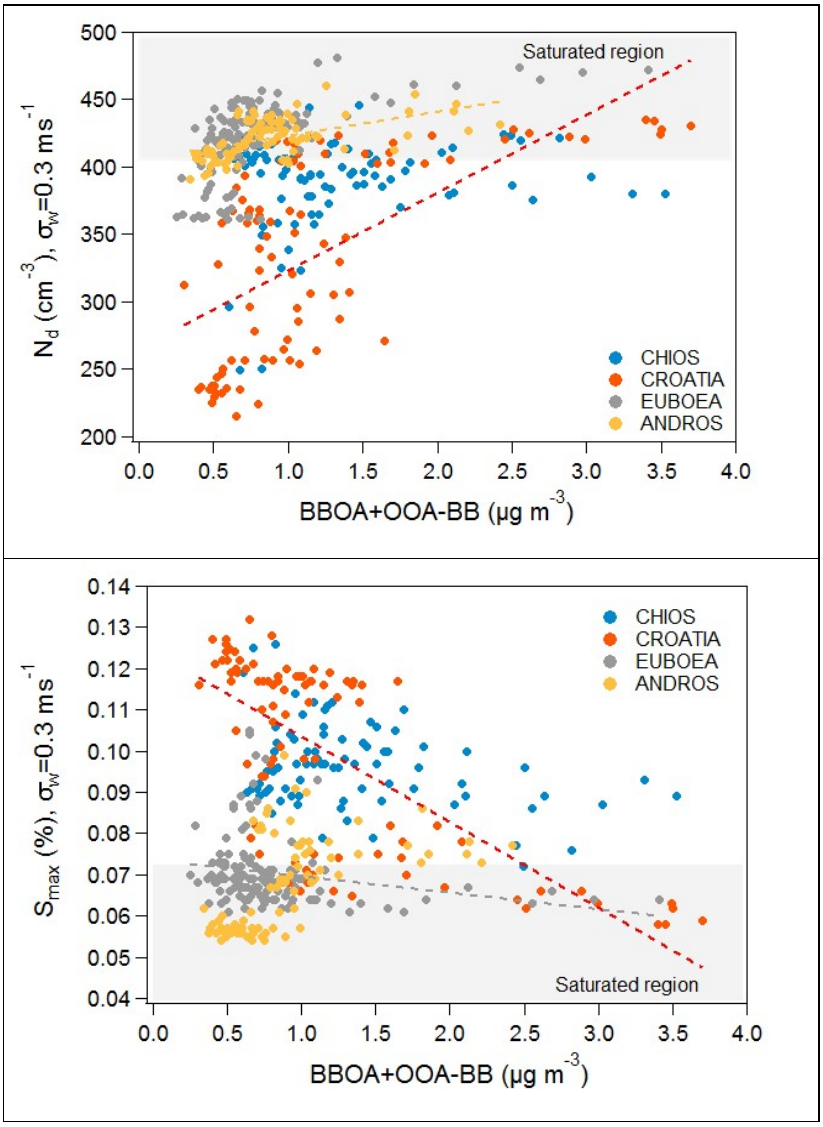
Saturated region
N_d (cm^-3), σ_w=0.3 ms^-1
500
450
400
350
300
250
200
CHIOS
CROATIA
EUBOEA
ANDROS
0.0
0.5
1.0
1.5
2.0
2.5
3.0
3.5
4.0
BBOA+OOA-BB (μg m^-3)
S_max (%), σ_w=0.3 ms^-1
0.14
0.13
0.12
0.11
0.10
0.09
0.08
0.07
0.06
0.05
0.04
CHIOS
CROATIA
EUBOEA
ANDROS
Saturated region
0.0
0.5
1.0
1.5
2.0
2.5
3.0
3.5
4.0
BBOA+OOA-BB (μg m^-3)